A viscosity regularized plasticity model for ceramics

Simons, E. C.; Weerheijm, J.; Sluys, L. J.

DOI
10.1016/j.euromechsol.2018.05.009

Publication date
2018

Document Version
Accepted author manuscript

Published in
European Journal of Mechanics, A/Solids

Accepted Manuscript

A viscosity regularized plasticity model for ceramics

E.C. Simons, J. Weerheijm, L.J. Sluys

PII: S0997-7538(17)30575-2

DOI: 10.1016/j.euromechsol.2018.05.009

Reference: EJMSOL 3609

To appear in: *European Journal of Mechanics / A Solids*

Received Date: 21 July 2017

Revised Date: 7 May 2018

Accepted Date: 9 May 2018

Please cite this article as: Simons, E.C., Weerheijm, J., Sluys, L.J., A viscosity regularized plasticity model for ceramics, *European Journal of Mechanics / A Solids* (2018), doi: 10.1016/j.euromechsol.2018.05.009.

A viscosity regularized plasticity model for ceramics

E.C. Simons[a], J. Weerheijm[a,b], L.J. Sluys[a]

[a] *Delft University of Technology, P.O. Box 5048, 2600 GA Delft, The Netherlands*
[b] *TNO, P.O. Box 45, 2280 AA Rijswijk, The Netherlands*

Abstract

Plasticity models are frequently used to describe ceramic materials. Well established and often used ceramic models are those by Johnson and Holmquist. These are softening plasticity models for which mesh dependency is a well known problem. A viscosity or rate dependency can be added to the material model to provide regularization and solve the mesh dependency problems. For the Johnson-Holmquist models a viscosity is proposed to work on the hydrostatic tensile strength. A consistency visco-plastic formulation is used. For the Johnson-Holmquist-2 model it is demonstrated that the proposed viscosity indeed removes the mesh dependency problems. This is shown for both quasi-static and dynamic loading. In addition it is shown that the proposed viscosity can predict an experimentally measured rate dependent spall strength of alumina ceramic, while the original model fails to do so.

Keywords: ceramic, Johnson-Holmquist, mesh-dependency, viscosity, quasi-static, dynamic

1. Introduction

Ceramic materials are frequently used in armour systems. Their high hardness and relative light weight make ceramics an ideal candidate for armour systems. Upon impact a projectile can deform heavily and may even fracture [1, 2, 3]. Directly underneath the projectile a zone of high compression and shear occurs. In this zone the ceramic may experience micro-cracking and crystal plasticity up to the point of full fragmentation. This zone is referred to as the 'comminuted' or 'quasi-plastic' zone, which can posses a considerable residual strength [4]. Some distance away from the projectile impact location the pressure drops and tensile states may be found at the ceramic surface. Ring cracks can be initiated, which may develop into cone cracks. These cone cracks form one of the main contributions to failure of ceramic armour. As a cone crack grows and reaches the back side of the armour, a plug is formed and the material has effectively lost its strength. Understanding the location and direction of these cone cracks is of great importance in armour design. Many experiments have been conducted to study these cone cracks in armour ceramics, both under dynamic [5, 6, 7, 8, 9, 10] and quasi-static loading [11, 12, 13].

To predict ceramic armour behaviour many material models have been developed over the years. Well known and often used material models are the phenomenological models by Johnson and Holmquist, who proposed three models: JH1 [14], JH2 [15] and JHB [16]. Another phenomenological model was proposed by Simha [17]. Other ceramic models are those by Rajendran and Grove [18], the dominant crack model by Zuo [19] and two models by Deshpande and Evans [20, 21]. This latter group of models is more theoretical and physical based than the first four phenomenological models. Although the latter group is appealing from a theoretical perspective in the current paper the JH2 model is used. This model is often used, simple in its formulation and is shown to correctly predict ceramic behaviour for a wide range of tests.

The ceramic models by Johnson and Holmquist are pressure dependent softening plasticity models. It is well known that softening plasticity models suffer from mesh dependency and the models by Johnson-Holmquist pose no exception. As a result these models may lead to spurious localization and a bias with respect to the discretization (i.e. mesh) when used in a finite element framework. Model results will not be objective with respect to the discretization

Email address: e.c.simons@tudelft.nl (E.C. Simons)

and vital failure mechanisms such as cone cracks may not be predicted correctly. This is detrimental for the predictive capabilities of these models with respect to armour performance.

To find objective results with respect to the discretization some form of regularization is required. Many methods have been described in literature which can regularize the results from softening plasticity models. Most methods regularize a solution by the introduction of a length scale This can be through the introduction of a specific type of non-local integral formulation [22] or a gradient formulation [23] in the evolution equation for plasticity. It is possible to provide regularization without directly introducing an explicit length scale in the material model. Introducing a rate dependency or viscosity can also provide regularization [24, 25, 26].

Simple and often used visco-plasticity formulations are those by Perzyna [27], Duvaut-Lions [28] and Wang [29]. The models by Perzyna and Duvaut-Lions are based on over-stress, which means that stress states outside the yield surface are allowed. The method by Wang is the so-called consistency formulation. In this formulation the yield surface is rate dependent and stress states are always inside or on the yield surface. For the Perzyna and Duvaut-Lions formulation the traditional Kuhn-Tucker loading conditions do not apply. However, for the consistency formulation one can still use the Kuhn-Tucker loading conditions.

For the Perzyna model it was recognized that the model may not converge to regular plasticity if multi-surface plasticity is used [30]. The Duvaut-Lions model does not have this problem and is therefore often used in literature. However, it can easily be shown that the model is unsuited to predict a full loss of deviatoric strength. This is because the model requires a converged inviscid solution, which is the so called backbone stress or strength. The viscous stress state is an interpolated value between the backbone and the trial stress state. For a non-zero deviatoric trial stress this will always lead to non-zero viscous stresses, even for a fully failed backbone material.

In the current paper a consistency formulation is used to regularize the JH2 material model with viscosity. Existing mesh dependency problems for the JH2 model will be illustrated using a tapered bar and a direct shear test. The original rate dependency of the JH2 model will be shown to be insufficient to provide regularization. A viscosity is proposed on the apex pressure (e.g. hydrostatic tensile strength) of the JH2 model. First a linear formulation is adopted for the apex viscosity. This is shown to regularize the solution of the tapered bar and the direct shear test. For high loading rates a linear viscosity may lead to an unrealistic failure zone size. An alternative mixed linear/logarithmic apex formulation is introduced. This mixed formulation is found to limit the failure zone size while still providing mesh independent results. The mixed linear/logarithmic viscosity is formulated such that a linear viscosity can be retrieved. The paper will end by showing how the spall strength varies as a function of loading rate in the original and proposed mixed linear/logarithmic viscosity formulation . It will be shown that the JH2 model with the proposed apex viscosity can correctly capture the rate dependent strength found in experiments, while the original model can not.

2. Methods and Models

To simulate ceramic behaviour the finite element method (FEM) is used. The FEM and required material models are implemented using the C++ based libraries from the open source package JemJive version 2.2 [31]. JemJive provides a FEM framework which supports both quasi-static and dynamic solution procedures in the form of a Newton-Raphson and Newmark solution scheme. The material models used to simulate ceramic behaviour are explained in the following subsections.

2.1. Material Models

2.1.1. Original model

The Johnson-Holmquist-2 (JH2) material model is a pressure dependent softening plasticity model. For a general softening plasticity model the yield function can be represented as a function $f(\boldsymbol{\sigma}, \boldsymbol{\kappa})$, where $\boldsymbol{\sigma}$ is the stress tensor and $\boldsymbol{\kappa}$ a collection of internal variables. In the JH2 model only a single scalar damage variable $D \in [0..1]$ is used as internal variable. The yield function for the JH2 model can thus be written as

$$f(\boldsymbol{\sigma}, D) = \sigma_{eq}(\boldsymbol{\sigma}) - \sigma_y(\boldsymbol{\sigma}, D). \tag{1}$$

The Von Mises equivalent stress $\sigma_{eq}(\boldsymbol{\sigma}) = \sqrt{3/2 \boldsymbol{s} : \boldsymbol{s}}$ is used, were $\boldsymbol{s} = \boldsymbol{\sigma} + p\boldsymbol{I}$ is the deviatoric stress tensor. The yield stress σ_y for JH2 model is defined as

$$\sigma_y^*(\boldsymbol{\sigma}, D) = (1 - D)\ \sigma_i^*(\boldsymbol{\sigma}) + D\, \sigma_f^*(\boldsymbol{\sigma}). \tag{2}$$

Here the superscript * indicates that the stress values are normalized with respect to the Hugoniot elastic limit σ_{HEL}. The subscripts i and f relate to the intact and failed (i.e. residual) material strengths

$$\sigma_i^*(\boldsymbol{\sigma}) = A\left(\frac{T + p(\boldsymbol{\sigma})}{P_{HEL}}\right)^n \left(1 + C\ln\dot{\bar{\epsilon}}_p^*\right), \tag{3}$$

$$\sigma_f^*(\boldsymbol{\sigma}) = B\left(\frac{p(\boldsymbol{\sigma})}{P_{HEL}}\right)^m \left(1 + C\ln\dot{\bar{\epsilon}}_p^*\right). \tag{4}$$

Here the material strength can be found as a function of the pressure $p(\boldsymbol{\sigma}) = -{}^1/_3\boldsymbol{\sigma} : \boldsymbol{I}$. The material's rate dependency can be scaled through parameter C, while a normalized equivalent plastic strain rate $\dot{\bar{\epsilon}}_p^* = \dot{\bar{\epsilon}}_p/\dot{\bar{\epsilon}}_p^0$ is used in the logarithmic formulation. For strain rates below the refence rate there is no rate effect (i.e. $C = 0.0$). Other model parameters are the reference strain rate $\dot{\bar{\epsilon}}_p^0$ and strength parameters A, B, n, m, P_{HEL} and T. The equivalent plastic strain rate is defined as

$$\dot{\bar{\epsilon}}_p = \sqrt{\frac{2}{3}\dot{\boldsymbol{e}}_p : \dot{\boldsymbol{e}}_p}, \tag{5}$$

where $\dot{\boldsymbol{e}}_p$ is the deviatoric plastic strain rate. From this equivalent plastic strain rate the rate of damage in the material can be found as

$$\dot{D} = \frac{\dot{\bar{\epsilon}}_p}{\bar{\epsilon}_p^{max}(\boldsymbol{\sigma})}, \tag{6}$$

where $\bar{\epsilon}_p^{max}(\boldsymbol{\sigma})$ is the maximum equivalent plastic strain for the given stress state. For pressures below the hydrostatic tensile strength T there is no gradual failure and full failure with $D = 1.0$ is immediately reached. For the Johnson-Holmquist models $\bar{\epsilon}_p^{max}$ is computed as

$$\bar{\epsilon}_p^{max}(\boldsymbol{\sigma}) = d_1\left(\frac{T + p(\boldsymbol{\sigma})}{P_{HEL}}\right)^{d_2}. \tag{7}$$

Here d_1 and d_2 are material parameters. Plastic deformation is obtained through the flow rule

$$\dot{\boldsymbol{\epsilon}}_p = \dot{\lambda}\, \partial g/\partial\boldsymbol{\sigma}, \tag{8}$$

where the JH2 model uses a plastic potential function

$$g = \sigma_{eq}(\boldsymbol{\sigma}) = \sqrt{\frac{3}{2}\boldsymbol{s} : \boldsymbol{s}}. \tag{9}$$

Two observations can be made on this plastic potential function. First, it can be shown that the volumetric plastic deformation $\epsilon_{V,p} = 0$, which implies isochoric plastic flow. Second, it can be shown that $\dot{\bar{\epsilon}}_p = \dot{\lambda}$.

Inelastic volumetric response is included in the JH2 model through a bulking contribution Δp to the pressure. This bulking formulation is explicit in nature, resulting in step size dependence. In the current paper bulking is not included.

2.1.2. Proposed model

Viscosity (i.e. rate dependency) can be used to regularize the finite element solution. The standard JH2 model has a rate dependency (viscosity) included in its formulation (see equations (3) and (4)). However, it will be shown in this paper that the standard rate dependency in the JH2 model is insufficient to provide satisfactory regularization.

A new rate dependency is proposed for the JH2 model. The proposed model will be referred to as the viscosity regularized JH2 model (JH2-V). The material strengths are reformulated from (3) and (4) to

$$\sigma_i^* = A\left(\frac{T(\dot{\bar{\epsilon}}_p) + p(\boldsymbol{\sigma})}{P_{HEL}}\right)^n, \tag{10}$$

$$\sigma_f^* = B\left(\frac{p(\boldsymbol{\sigma})}{P_{HEL}}\right)^m. \tag{11}$$

In this formulation the equivalent plastic strain rate $\dot{\bar{\epsilon}}_p$ is used to scale the material's ultimate tensile limit T of the intact material strength. Note that the original logarithmic scaling $(1 + C\ln\dot{\bar{\epsilon}}_p^*)$ from equations (3) and (4) is absent in this proposed formulation. The proposed scaling of the ultimate tensile limit does not exclude the original rate dependency, both formulations may be used simultaneously. However, in the current paper the original JH2 rate dependency and the proposed rate dependency on the ultimate tensile limit will not be used simultaneously in order to study their effects independently.

In the consistency formulation a yield function $f(\boldsymbol{\sigma}, \boldsymbol{\kappa}, \dot{\boldsymbol{\kappa}})$ can be defined. Here $\dot{\boldsymbol{\kappa}}$ is the rate of some internal variables. In the proposed material model only the rate of a single internal variable $\dot{\kappa}$ is used. Here $\dot{\kappa} = \dot{\bar{\epsilon}}_p = \dot{\lambda}$, which is the rate of the plastic multiplier. Using the consistency formulation function (1) can now be written as

$$f_{rd}(\boldsymbol{\sigma}, D, \dot{\lambda}) = \sigma_{eq}(\boldsymbol{\sigma}) - \sigma_y(\boldsymbol{\sigma}, D, \dot{\lambda}), \tag{12}$$

which will be referred to as the rate dependent yield function. This is in accordance with the consistency model and the Kuhn-Tucker loading conditions

$$f_{rd} \leq 0, \qquad \dot{\lambda} \geq 0, \qquad \dot{\lambda} \cdot f_{rd} = 0 \tag{13}$$

still apply.

The rate dependency of the ultimate tensile pressure is initially assumed in a linear form

$$T(\dot{\bar{\epsilon}}_p) = T(\dot{\lambda}) = T_0 + \eta\dot{\lambda}, \tag{14}$$

where η is the viscosity and T_0 the original rate independent strength parameter. The current viscosity is proposed to provide regularization. The initial choice for a linear rate dependency will be critically reviewed in section 5. Recent experimental work indicates that there is also a physical component to this rate effect on the tensile strength of ceramics [32] [33]. It will also be investigated in section 5 how the proposed rate dependency affects the predicted tensile strength.

The original and the proposed rate dependencies are visualized in Figure 1. It is clear from Figure 1a that the original rate dependency provides a deviatoric scaling of the material strength. The apex point T is left unaltered by the original rate dependency. From Figure 1b it may be observed that the proposed rate dependency provides a hydrostatic shift of the yield function with the loading rate. It is important to note the effect of both rate dependencies over the range of pressures. For the original rate dependency the absolute strength increase is found to be largest for higher pressures. For the proposed rate dependency the opposite holds true, as the largest absolute strength increase is found at the original apex point T.

Other types of rate dependency may be obtained by performing a similar scaling on different model parameters. Although this may work for the other JH material models it will not work for the JH2 model. This is due to the singularity at the apex. Scaling for instance A with rate will only provide a deviatoric scaling and will not give the desired increase in strength under tension. The proposed formulation on the apex pressure is however more general and a similar approach can also be used for the other JH models.

3. Algorithmic aspects

For plasticity models the strain rate can be split into an elastic and plastic component

$$\dot{\boldsymbol{\epsilon}} = \dot{\boldsymbol{\epsilon}}_e + \dot{\boldsymbol{\epsilon}}_p. \tag{15}$$

The stress rate is expressed as

$$\dot{\boldsymbol{\sigma}} = \boldsymbol{D}_e\dot{\boldsymbol{\epsilon}}_e = \boldsymbol{D}_e\left(\dot{\boldsymbol{\epsilon}} - \dot{\boldsymbol{\epsilon}}_p\right), \tag{16}$$

where the elastic stiffness tensor $\boldsymbol{D}_e$ is used. Application of the flow rule (8) results in

$$\dot{\boldsymbol{\sigma}} = \boldsymbol{D}^e\left(\dot{\boldsymbol{\epsilon}} - \dot{\lambda}\frac{\partial g}{\partial \boldsymbol{\sigma}}\right) = \boldsymbol{D}^e\left(\dot{\boldsymbol{\epsilon}} - \dot{\lambda}\boldsymbol{m}\right). \tag{17}$$

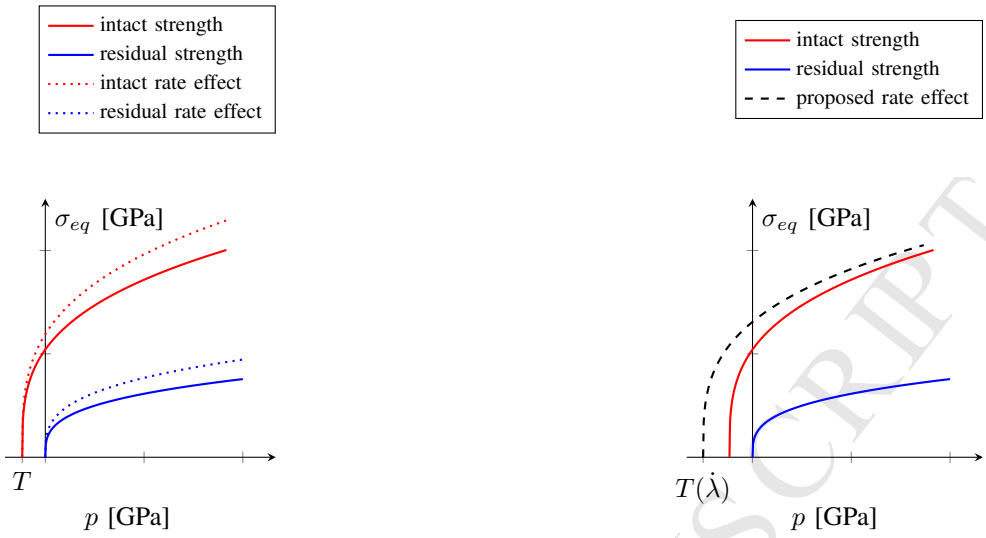

(a) Original rate effect

(b) Proposed rate effect

Figure 1: Deviatoric strength σ_{eq} of the Johnson-Holmquist-2 material model plotted as function of pressure p. Figures show the original and proposed rate effects. Note the relatively large increase in strength under tension and the minimal increase under compression for the proposed model.

In this formulation $\dot{\lambda}$ is the rate of plastic multiplier, while $\boldsymbol{m} = \partial g/\partial \boldsymbol{\sigma}$ is the flow direction with the plastic potential function g. In the current paper the plastic potential function from (9) is used where g is only a function of deviatoric stress. It is also possible to define a plastic potential function which depends on the full stress tensor, which includes a hydrostatic component. One may, for instance, use associative plasticity ($g = f$), which introduces volumetric inelastic deformation [34].

Rate equations cannot be used directly in the discrete formulation of the finite element method. The relations above can be written in incremental form, where the stress increment reads

$$\Delta\boldsymbol{\sigma} = \boldsymbol{D}^e \left(\Delta\boldsymbol{\epsilon} - \Delta\lambda \boldsymbol{m}\right). \tag{18}$$

A new stress can now be found as

$$\begin{aligned} \boldsymbol{\sigma}^{n+1} &= \boldsymbol{\sigma}^n + \Delta\boldsymbol{\sigma}, \\ &= \boldsymbol{D}^e \left(\boldsymbol{\epsilon}^n - \boldsymbol{\epsilon}_p^n\right) + \boldsymbol{D}^e \left(\Delta\boldsymbol{\epsilon} - \Delta\lambda \boldsymbol{m}\right), \\ &= \boldsymbol{D}^e \left(\boldsymbol{\epsilon}^{n+1} - \boldsymbol{\epsilon}_p^n - \Delta\lambda \boldsymbol{m}\right). \end{aligned} \tag{19}$$

Here n and $n+1$ refer to the previous and current load increment. The unknowns in this incremental form are: the new stress $\boldsymbol{\sigma}^{n+1}$ and the increment of plastic multiplier $\Delta\lambda$. For simple plasticity models a closed form solution to this plastic multiplier is known and it can be computed directly from the given strain increment. For more complex plasticity formulations which include non-linearities, such as the JH2 model, a close form expression usually does not exist. For these cases an iterative scheme can be used at integration point level to find the correct stress and plastic multiplier. In the current paper an Euler backward formulation is used [35].

3.1. Plasticity or elasticity

When a new global load increment is performed the new stress and internal states have to be determined at integration point level. For an integration point a trial stress state is computed under the assumption of elastic loading ($\Delta\lambda = 0$). From (19) this trial state can be computed as

$$\boldsymbol{\sigma}^{tr} = \boldsymbol{D}^e \left(\boldsymbol{\epsilon}^{n+1} - \boldsymbol{\epsilon}_p^n\right). \tag{20}$$

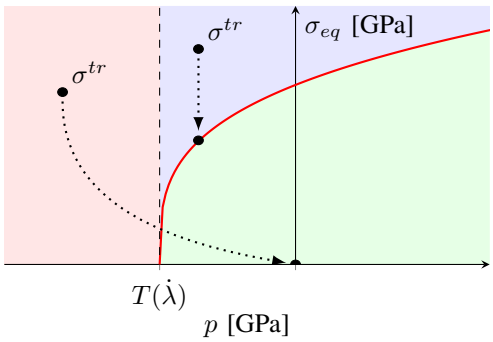

Figure 2: Return mapping for the JH2 model visualized. Any trial state in the green stress space remains elastic, in the blue stress space regular return mapping is applied while the red domain requires apex return.

Using this trial stress the yield function from (12) can be evaluated. A yield function $f_{rd} < 0$ results in elastic deformation of the material, while $f_{rd} \geq 0$ will result in plastic deformation. For the consistency model the initial check for plasticity is based on $f_{rd}(\boldsymbol{\sigma}^{tr}, D^n, 0.0)$. Here D^n is the final damage predicted by the previous load increment and an initial rate $\dot{\lambda} = 0.0$ is assumed. This is in line with the assumption of an elastic trial step (i.e. $\Delta\lambda = 0$).

For plastic deformation in the JH2 material model there are two domains in the stress space of interest, each with a specific algorithmic treatment. The first domain is where the trial stress can be returned to the yield surface in the flow direction $\partial g/\partial\boldsymbol{\sigma}$. In this stress domain the Euler backward return mapping scheme can be used to find the new stress state $\boldsymbol{\sigma}^{n+1}$ and increment in plastic multiplier $\Delta\lambda$. The second stress domain is where the trial stress can not be returned to the yield surface in the flow direction $\partial g/\partial\boldsymbol{\sigma}$. For the JH2 model with plastic potential (9) this includes all states with $p^{tr} < T$. Once the material is fully failed (i.e. $D = 1$) the apex point shifts to a zero pressure and the check becomes $p^{tr} < 0$. To find an admissible stress for this second group of trial states requires the use of a so-called apex return. The three domains in the stress space (two plastic and one elastic) are also visualized in Figure 2, where the blue domain indicates regular return, the red domain apex return and the green domain indicates an elastic state.

The proposed check for apex return has some limitations. The check only works for a pure deviatoric flow rule where it is known that $p^{tr} = p^{n+1}$. If volumetric plastic deformation would be included through the plastic potential function $p^{tr} \neq p^{n+1}$, which means the check $p^{tr} < T$ is no longer conclusive for apex return. Also if the material reaches full damage (i.e. $D = 1$), the apex pressure reduces to zero and the the check $p^{tr} < T$ is no longer valid. Finally, if rate dependency is considered on the apex also a different check is required, since the trial rate was assumed to be zero and $T(0.0) \neq T(\dot{\lambda}^{n+1})$ for any $\dot{\lambda}^{n+1} > 0$.

A more robust approach is to assume regular return mapping and check for a violation of the apex criterion $p^{n+1} < T(\dot{\lambda}^{n+1})$ in every Euler backward iteration. If the apex criterion is violated, a switch to apex return is necessary. This algorithmic treatment is shown in Box 1. The exact formulation of the apex return scheme is discussed in 3.3.

3.2. Regular return algorithm

An Euler backward scheme is used for the regular return mapping algorithm. For a visco-plastic model in the consistency formulation this can be used to find a solution of (19). The derivation and formulation of an Euler backward scheme for such a model has already been discussed in literature [29], it will therefore not be repeated in the current paper.

3.3. Apex return algorithm

When the apex check is violated regular return mapping can no longer be applied. This can be found from (9), which shows the original JH2 model only allows deviatoric plastic strain. Therefore the plastic flow cannot result in an increase of pressure and a point inside the yield surface is never reached. Full failure is immediately applied (i.e. $D = 1$) and the stress is mapped to the apex of the residual strength curve at $p = 0$. The new stress state will be

$$\boldsymbol{\sigma}^{n+1} = \mathbf{0}. \tag{21}$$

compute ϵ^{n+1} from $\boldsymbol{u}^{n+1}$
compute $\boldsymbol{\sigma}^{tr}$
initialize $D^{n+1} = D^n$ and $\dot{\lambda}^{n+1} = 0.0$
if $f_{rd}(\boldsymbol{\sigma}^{tr}, D^{n+1}, \dot{\lambda}^{n+1}) \geq 0$
PLASTIC DEFORMATION:

1. start with:
   → REGULAR RETURN MAPPING
2. if $p^{n+1} < T(\dot{\lambda}^{n+1})$ or ($p^{n+1} < 0$ and $D^{n+1} = 1$):
   → APEX RETURN

else
ELASTIC DEFORMATION:

1. $\boldsymbol{\sigma}^{n+1} = \boldsymbol{\sigma}^{tr}$

Box 1: Elastic or plastic loading

Table 1: JH2 and JH2-V material properties

variable	value	unit	variable	value	unit	variable	value	unit
E	375.0	GPa	C	0.0 or 0.025	-	σ_{HEL}	0.3746	GPa
ν	0.0	-	T	0.2	GPa	d_1	0.05	-
ρ	3700	kg/m^3	n	0.6	-	d_2	0.0	-
A	0.930	GPa	m	0.6	-		-	
B	0.310	GPa	P_{HEL}	0.1250	GPa			

The consistent tangent for this returned stress is easy to compute as

$$\boldsymbol{D}^{vp} = \boldsymbol{0}. \tag{22}$$

Finally, the plastic deformation under apex return has to be assigned. It was already mentioned that the JH2 model only predicts pure deviatoric plastic flow. For a fully failed material under tension no deviatoric strength is present. From (19) it can be found that zero deviatoric stress is predicted if

$$\Delta\boldsymbol{\epsilon}_p = \boldsymbol{e}_e^{n+1}. \tag{23}$$

This reduces the deviatoric stress to zero and also satisfies the purely deviatoric flow rule for the JH2 model.

4. Results

The material models presented in section 2.1 are used to simulation a number of test cases. Each test case will be simulated using the JH2 model with $C = 0.0$ (JH2ri), the JH2 model with $C = 0.025$ (JH2-rd) and the viscosity regularized JH2 model (JH2-V). Other material properties are shown in Table 1. The values of P_{HEL} and σ_{HEL} are obtained by choosing $\mu_{HEL} = 0.001$. Note that by choosing $d_2 = 0.0$ the failure strain becomes independent of pressure. This ensures a finite rate of damage in the JH2-V model for pressures below the static apex pressure T.

The aim of the simulations in the current section is threefold. First, the simulations will show mesh dependency for the JH2 model. Second, the results show that the JH2-rd model has regularizing properties but these are insufficient for some loading cases. Third, the JH2-V model is shown to properly regularize the simulation results for all reviewed loading cases.

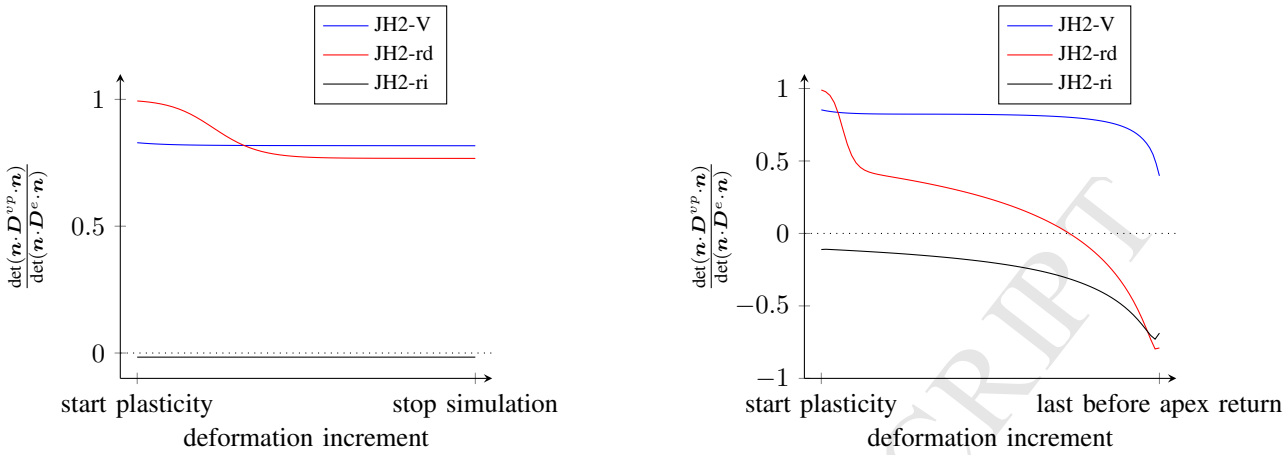

(a) Shear loading

(b) Tensile loading

Figure 3: Single element tested under pure shear and uniaxial tension. The graphs show the normalized determinant of the acoustic tensor. A negative value indicates a loss of ellipticity of the boundary value problem. This will lead to mesh-dependent results.

4.1. Unit test

Mesh-dependency is a result of the loss of ellipticity of the boundary value problem in static analyses [36]. It can be shown mathematically when this loss of ellipticity occurs. An acoustic tensor is defined as

$$\boldsymbol{A} = \boldsymbol{n} \cdot \boldsymbol{D}^{vp} \cdot \boldsymbol{n}, \tag{24}$$

where $\boldsymbol{n}$ is a normal vector to a (localized) failure surface and $\boldsymbol{D}^{vp}$ the (visco)plastic tangent matrix. Loss of ellipticity occurs if

$$\det(\boldsymbol{A}) \leq 0, \tag{25}$$

for any or some $\boldsymbol{n}$. The current paper will not provide proof for the loss of ellipticity in the JH2 model nor for the sustained ellipticity in the JH2-V model. Instead a numerical investigation with single element tests is adopted.

A single Q4 plane strain element with a single Gauss integration point is subjected to pure shear or pure uniaxial tensile deformation. The deformation is incrementally increased to allow for plastic deformation of the material and possibly invoking apex return. For each load increment in which the integration point experiences plastic deformation the visco-plastic tangent matrix is stored. Assuming a normal vector $\boldsymbol{n}$ in the plane of the element with an in-plane orientation varying from $\phi = 0°,\ 1°, .. 180°$ the acoustic tensor can be computed for each direction. During plastic deformation one or more directions may show a negative determinant, indicating loss of ellipticity. Note that for apex return (22) holds, thus $\det(\boldsymbol{A}) = 0$ and the material will lose ellipticity.

Figure 3 shows the minimum values for the determinant of the acoustic tensor found during unit testing. The vertical axes show the values of the determinant normalized with respect to the determinant of the elastic acoustic tensor. Figure 3a shows the results for the shear test. The horizontal axis represents the increments from start of plastic deformation to the end of the simulation, full failure (i.e. $D = 1.0$) was not reached during this shear test. The JH2-ri model shows a negative determinant for all plastic load steps. This was to be expected as softening plasticity models are known to lead to loss of ellipticity. The addition of a rate dependency either in form of JH2-rd or JH2-V model regularizes the model and ensures a positive determinant of the acoustic tensor. Figure 3b presents the unit test results under tension. Again the horizontal axis represents the increments during the simulation, this time from the start of plasticity to the step just before apex return. These results show that both the JH2-ri and JH2-rd models lose ellipticity during loading. For the JH2-V model ellipticity is maintained during plastic deformation.

The unit test shows that the JH2-rd model can provide regularization, but not for all loading cases. The JH2-V model does provide regularization under the investigated loading scenarios. In the next subsections the mesh-dependency resulting from the loss of ellipticity will be shown. Initial results focus on spurious localization, while later results focus on mesh-bias.

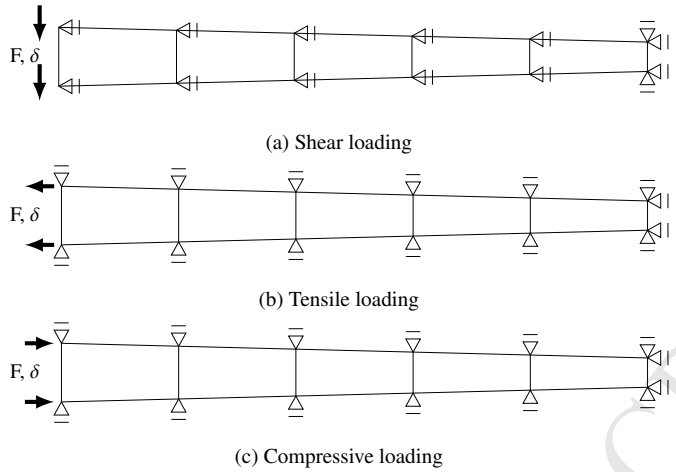

(a) Shear loading

(b) Tensile loading

(c) Compressive loading

Figure 4: Schematic representation of tapered bar tests. Boundary conditions are shown, the triangles represent a fixed degree of freedom, the arrows indicate the direction of loading.

4.2. Tapered bar cases

The first test case is a tapered bar subjected to shear, tensile or compressive loading. The bar has a length of 5mm and a width ranging from 1.0-1.1mm. For a tapered bar failure is expected to initiate in the smallest and thus weakest cross section of the bar. Figure 4 shows a schematic view of the three tapered bar tests, including the boundary conditions. A deformation δ is applied on the left boundary and a reaction force F is measured.

In all simulations a plane strain formulation is used for the tapered bar. Four noded quadrilateral elements are used with a 2∗2 Gaussian integration scheme. The number of elements is variable, to study mesh dependency 5, 10 and 20 equidistributed elements are used. The displacement is applied in increments of $\Delta u = 1.0 \cdot 10^{-5}$mm. When viscous models are considered a time step is introduced as $\Delta t = 1.0 \cdot 10^{-4}$ms. This ensures a loading rate of 0.1m/s. Although the viscous cases have a time step involved, the loading is quasi-static and inertia effects are excluded from the simulation.

An adaptive load stepping scheme is adopted in order to obtain convergence. In this scheme the previously mentioned increment in displacement is reduced or increased depending on the convergence of the global Newton-Raphson scheme [35]. A constant rate of loading is maintained by scaling the time increment in the same way as the displacement increment.

4.2.1. Tapered bar under shear

The tapered bar case under shear from Figure 4a is simulated using the JH2-ri model. Figure 5a shows the resulting equivalent plastic strain of the tapered bar after 10μm of deformation. From top to bottom 5, 10 and 20 elements are used. The figure clearly shows localization of plastic deformation in a single element. This is confirmed by Figure 5c, where the equivalent plastic strain is plotted along the bar axis. The load displacement data for these simulations are shown in Figure 5b. This confirms the mesh dependency once more, as a finer mesh results in a more brittle response.

A second series of simulations was performed using the new JH2-V model. A viscosity parameter $\eta = 0.2 \cdot 10^{-3}$ GPa·s is chosen such that the plastic deformation occurs in a finite zone. Figure 6a shows the resulting equivalent plastic strain of the tapered bar after 10μm of total deformation, which confirms the finite zone of plastic deformation. Figures 6b and 6c confirm that the plastic zone size has converged for the given range of elements. Compared to the 20 element JH2-ri results (black dotted line in Figure 6b) a 3.16% increase of peak load is found.

A third series of simulations is performed with the standard JH2-rd model. The rate parameter $C = 0.025$ is chosen such that the plastic deformation occurs in a finite zone. Figure 7a shows the resulting plastic deformation of the tapered bar after 10μm of total deformation. From the figures it can be found that the plastic deformation indeed spreads over a zone rather than localizing in a single element (as was observed for the JH2-ri model). Although the JH2-rd model shows a zone of plastic deformation, the size of this zone still appears to change as the mesh is refined from 10 to 20 elements (Figure 7a). Only when the 40 element mesh is compared to the 20 element mesh, the zone

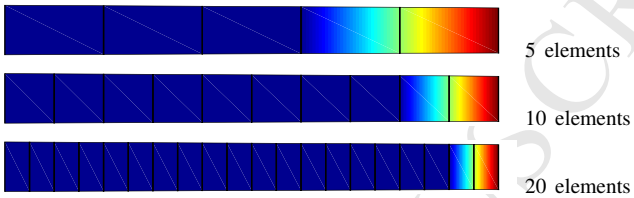

(a) Equivalent plastic strain. Localization upon mesh refinement is clearly visible.

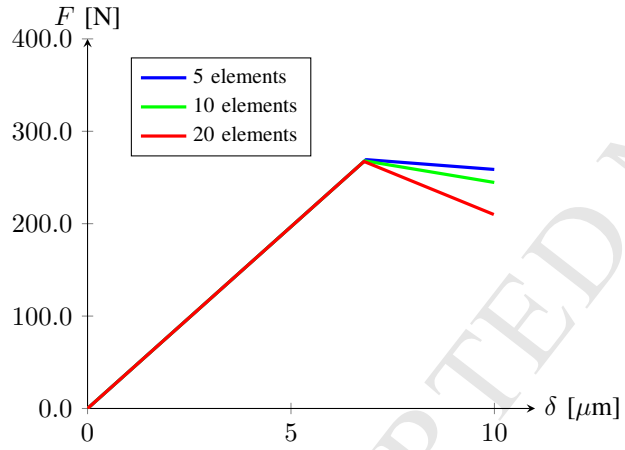

(b) Force displacement graph. Localization upon mesh refinement is clearly visible.

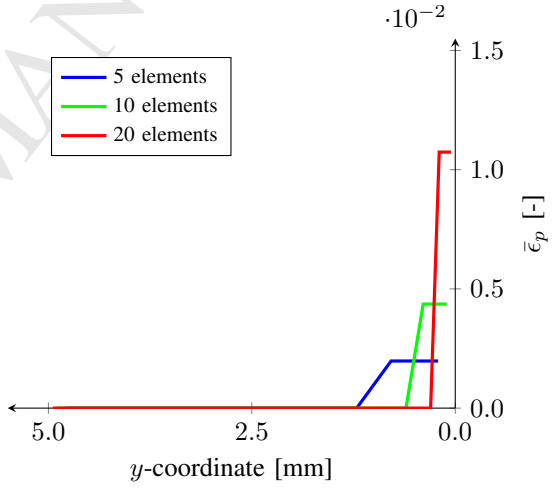

(c) Equivalent plastic strain profile along the tapered bar axis. An increase in equivalent plastic strain can be found for decreasing mesh size.

Figure 5: Tapered shear bar results for the JH2-ri model.

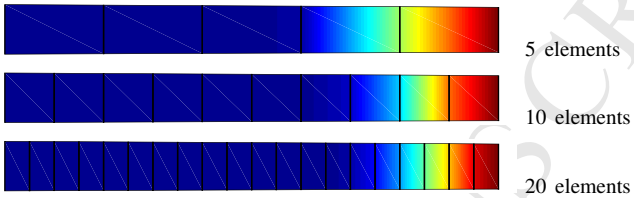

(a) Equivalent plastic strain. Viscosity parameter η is chosen such that regularization is observed. Plastic deformation is found to spread over a zone rather than to localize.

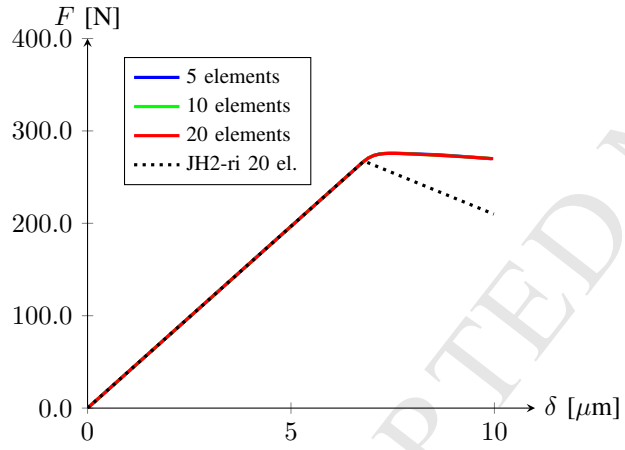

(b) Force displacement graph. All three meshes give similar results. Small increase of strength is observed compared to the JH2-ri model.

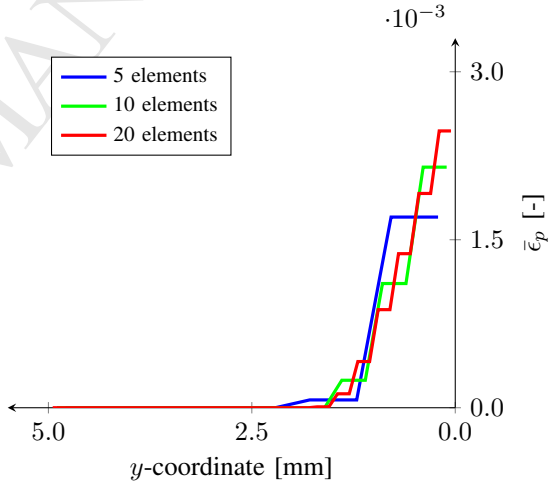

(c) Equivalent plastic strain plotted along the tapered bar axis. The profiles are found to converge upon mesh refinement.

Figure 6: Tapered shear bar results for the JH2-V model.

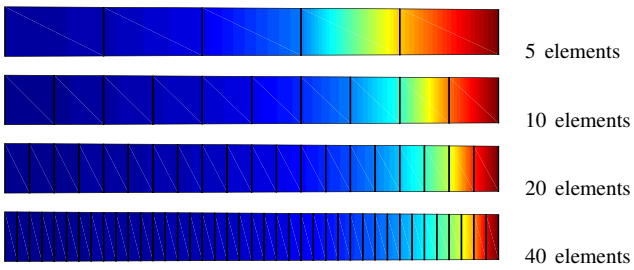

(a) Equivalent plastic strain. Rate dependency parameter C is chosen such that regularization is observed. Plastic deformation is found to spread over a zone rather than to localize.

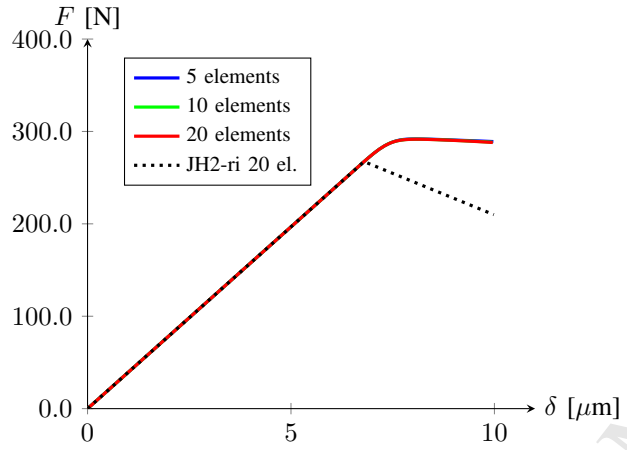

(b) Force displacement graph. All three meshes give similar results. Small increase of strength is observed compared to the JH2-ri and JH2-V model.

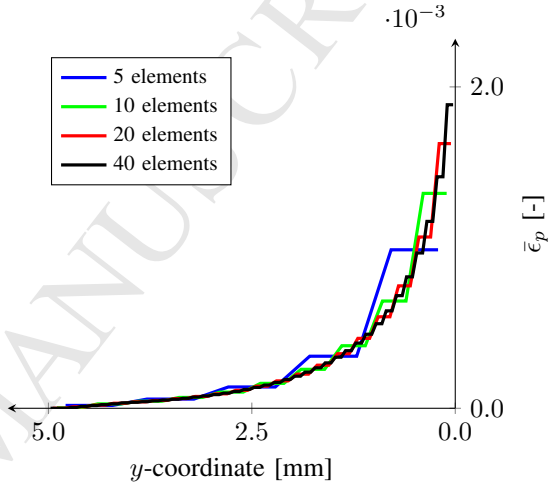

(c) Equivalent plastic strain plotted along the tapered bar axis. The profiles are found to converge upon mesh refinement.

Figure 7: Tapered shear bar results for the JH2-rd model.

appears to be somewhat similar in size. This is confirmed by the equivalent plastic stain profile in Figure 7c. It is interesting to note that the plastic zone spreads through the entire bar for the JH2-rd model. The load displacement data in Figure 7b shows equal responses for the 5, 10 and 20 element meshes. The increase of peak force is 9.11% compared to the JH2-ri model. This is significantly more than the 3.16% found for the JH-V model.

To compare the plastic zone predicted by the JH2-ri , JH2-rd and JH2-V models the normalized equivalent plastic strain profiles are plotted along the bar axis. Figure 8 shows the integration point values of this normalized equivalent plastic strain. The 20 element mesh is used for this comparison. A stepwise profile can be observed for all three cases. This is the result of the use of linear elements, which are only capable of predicting a constant strain in a single element. The figure shows a localized plastic deformation of the JH2-ri model. For the JH2-rd and JH2-V model plastic deformation is found to occur in a zone rather than a single element. The plastic deformation zone of the JH2-rd model is found to extend throughout the entire bar, while the plastic zone of the JH2-V model is smaller.

4.2.2. Tapered bar under tension

A simulation of the tapered bar under tension from Figure 4b is conducted using the JH2-ri model. Figure 9a shows the resulting plastic deformation of the tapered bar, discretized with 5, 10 and 20 elements. Similar to the shear loaded bar the plastic deformation localizes in a single element. Neighbouring elements show no plastic deformation. The equivalent plastic strain profiles from Figure 9c confirm this. All three meshes are found to have the same amount of equivalent plastic strain. This is because an arc-length method is used and all elements follow the exact same stress strain path.

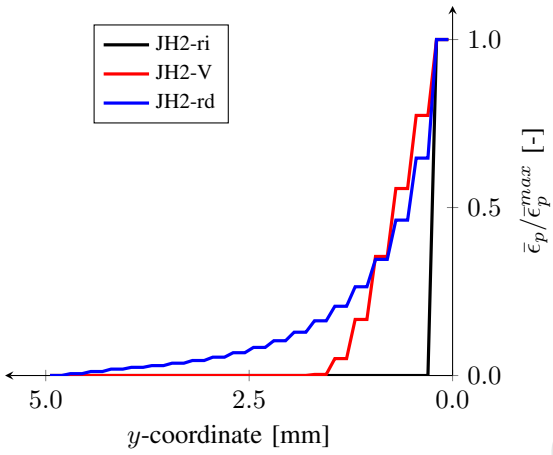

Figure 8: Normalized equivalent plastic strain plotted along the tapered bar axis. The 20 element mesh is used, results are for three different material models.

Arc-length control is used in these simulations to be able to trace snap-back behaviour. This is typical for brittle materials and results from the softening behaviour of the material. As plasticity localizes in a single element other elements are found to unload elastically. This reduces the total force on the bar and also the total deformation to reach this force. The load displacement graph for the tensile bar is shown in Figure 9b. The snap-back is clearly seen in the figure. As soon as plastic deformation is initiated the force is reduced and continues to reduce until the element has fully failed. A sudden drop in force is observed when the pressure in the weakest element reaches the apex pressure T, after which apex return is invoked and negative pressures can no longer be supported. Again, similar to the shear case, the curves do not converge when the mesh is refined and mesh-dependency is clearly shown.

A second series of simulations is performed on the tapered tensile bar with the JH2-V model. Figure 10a shows the resulting plastic deformation of the tapered bar right before apex return is invoked. In the tapered bar with the JH2-V model apex return will only be invoked in the weakest element, similar to the JH2-ri model. Showing the equivalent plastic deformation after this apex return would give the impression of mesh-dependency, as the magnitude of equivalent plastic strain in this weakest element under apex return is considerably larger than in neighbouring elements. Showing the equivalent plastic strain before apex return correctly shows the mesh-independence of the model. This mesh-independence is confirmed by the equivalent plastic strain profiles shown in Figure 10c. For the JH2-V model the arc-length method can not be used, and therefore the peak values of equivalent plastic strain are not exactly the same for all meshes. The figure shows plastic deformation spreading over a zone rather than localizing in a single element. The load displacement in Figure 10b again confirms the mesh independent behaviour of the JH2-V model. The peak load of the JH2-V model is found to be 4.47% higher than the JH2-ri peak load.

A third and final series of simulations is performed on the tapered tensile bar, using the JH2-rd model. Recall that the rate dependency parameter $C = 0.025$ was chosen such that the results under shear were regularized. Figure 11b shows the load displacement graph for the JH2-rd model. The peak load of the JH2-rd model is found to be 5.94% higher than the JH2-ri peak load. Compared to the JH2-V results the post peak deformation is smaller and the behaviour appears to be more brittle. Figure 11a shows the equivalent plastic strain plots for the tapered bar under tension. Similar to the results from the JH2-V model the equivalent plastic strain is plotted before apex return. The plastic deformation no longer spreads over a zone comparable to the shear case. The figure suggests that plastic deformation is localized in the last element of the bar. However, close examination of integration point data in Figure 11c reveals that the plastic deformation does spread to neighbouring elements, although most deformation occurs in the last element of the bar. The peak value of the equivalent plastic strain may be found to reduce upon mesh refinement. Since plastic strain is related to energy dissipation it is clear that reducing the mesh size also reduces the dissipated energy in the system. Next to (spurious) localization this is one characteristic of mesh dependency. So although the value of $C = 0.025$ appears to regularize the solution for the tapered bar under shear, it may not provide regularization under tensile loading. This would be in line with the unit test results from section 4.1, which

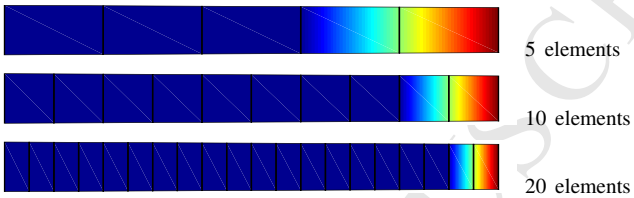

(a) Equivalent plastic strain. Localization upon mesh refinement can be seen clearly.

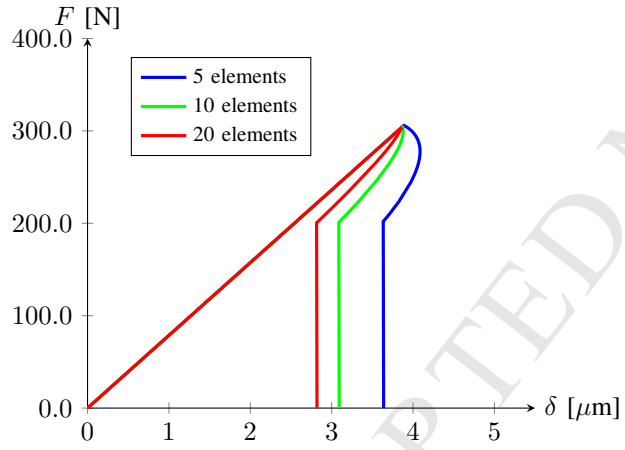

(b) Force displacement graph. Localization upon mesh refinement is clearly visible.

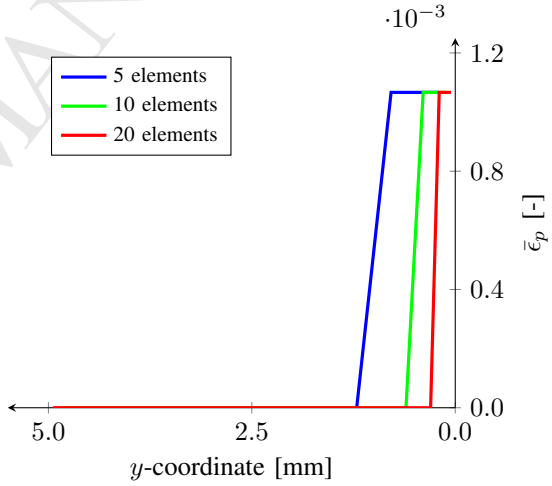

(c) Equivalent plastic strain profile along the tapered bar axis. The equivalent plastic strain can be found to be equal for all mesh sizes.

Figure 9: Tapered tensile bar results for the JH2-ri model.

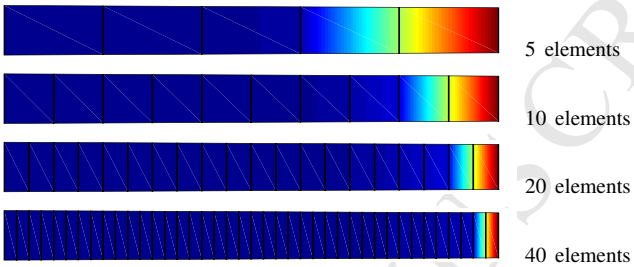

(a) Equivalent plastic strain. Plastic deformation is bound to a zone rather than a single element.

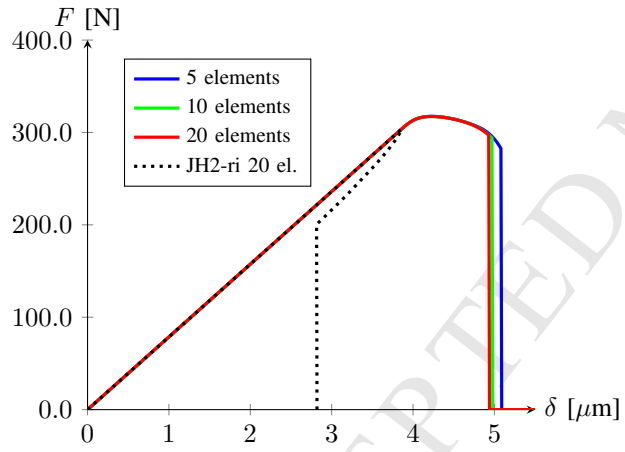

(b) Force displacement graph. All three meshes give similar results. Small increase of strength is observed compared to the regular JH2-ri model.

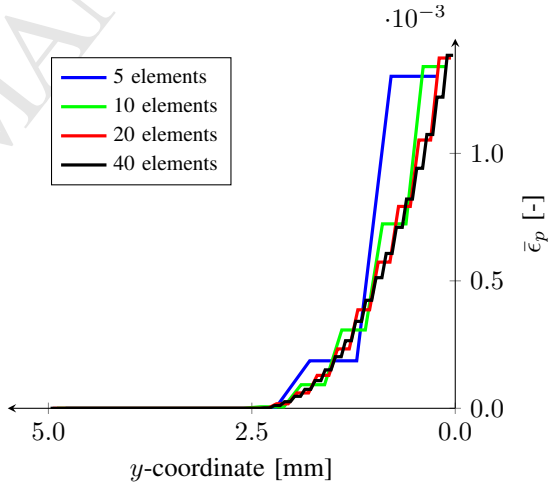

(c) Equivalent plastic strain plotted along the tapered bar. Profiles are found to converge upon mesh refinement.

Figure 10: Tapered tensile bar results for the JH2-V model.

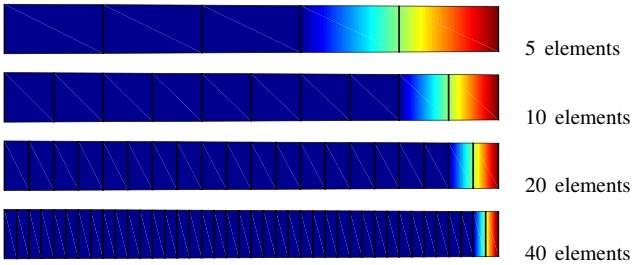

(a) Equivalent plastic strain. Localization upon mesh refinement can be observed, although a small amount of plasticity is found to spread over neighbouring elements. This is in contrast with the shear case, where regularized results were found.

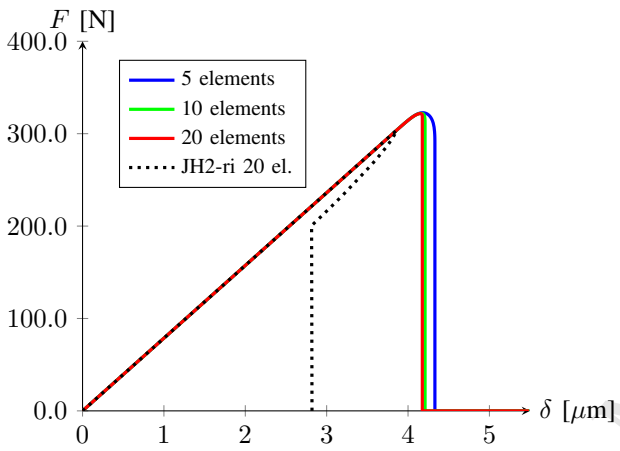

(b) Force displacement graph. Small increase of strength is observed compared to the JH2-ri and JH2-V model.

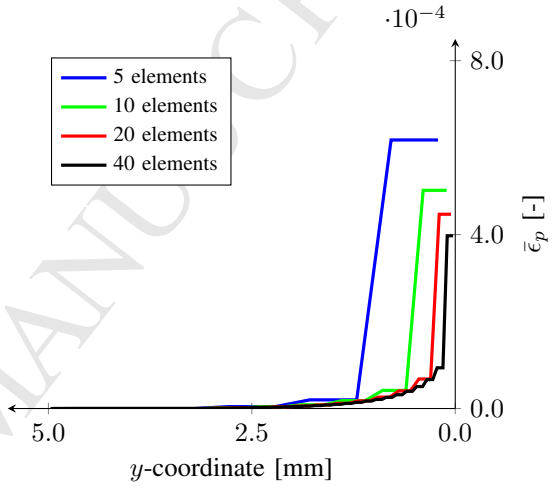

(c) Equivalent plastic strain plotted along the tapered bar. The profiles do not converge for the current meshes.

Figure 11: Tapered tensile bar results for the JH2-rd model. Rate dependent parameter C is equal to the tapered shear bar case. Recall that results were regularized under shear for the chosen C parameter.

showed that ellipticity was lost for the JH2-rd model under tension but not under shear. To confirm these findings the determinant of the acoustic tensor is computed during the tapered bar test. For this purpose a single integration point in the smallest element at the right side of the bar (Figure 4) is analyzed. The normalized values of the determinant of the acoustic tensor are presented in Figure 12. Both the results for the JH2-rd and the JH2-V model are presented. Ellipticity is lost if condition (25) is met. The results once more show that the JH2-rd model loses ellipticity, while the JH2-V model retains ellipticity throughout the simulations. For the JH2-rd model oscillations in the value of the determinant of the acoustic tensor are observed if the value approaches zero. These oscillations are related to reductions of the step size by the adaptive load stepping scheme.

For a more thorough comparison the normalized equivalent plastic strain profiles are compared in Figure 13. The 20 element mesh is used for this comparison. Similar to the shear cases the JH2-ri model shows spuriously localized plastic deformation, while the JH2-rd and the JH2-V models show a zone of plastic deformation. When both viscous models are compared by means of the normalized profiles, the sharpest profile is found for the JH2-rd model. Although this model predicts a zone of plastic deformation, most deformation still occurs in the last element. This explains why the plot in Figure 11a appears to have localized plastic deformation.

4.2.3. Tapered bar under compression

As a final check in the tapered bar under compression from Figure 4c is studied. The equivalent plastic strain profile for the JH2-ri model is shown in Figure 14a. Under compression the plastic deformation is found to occur in a

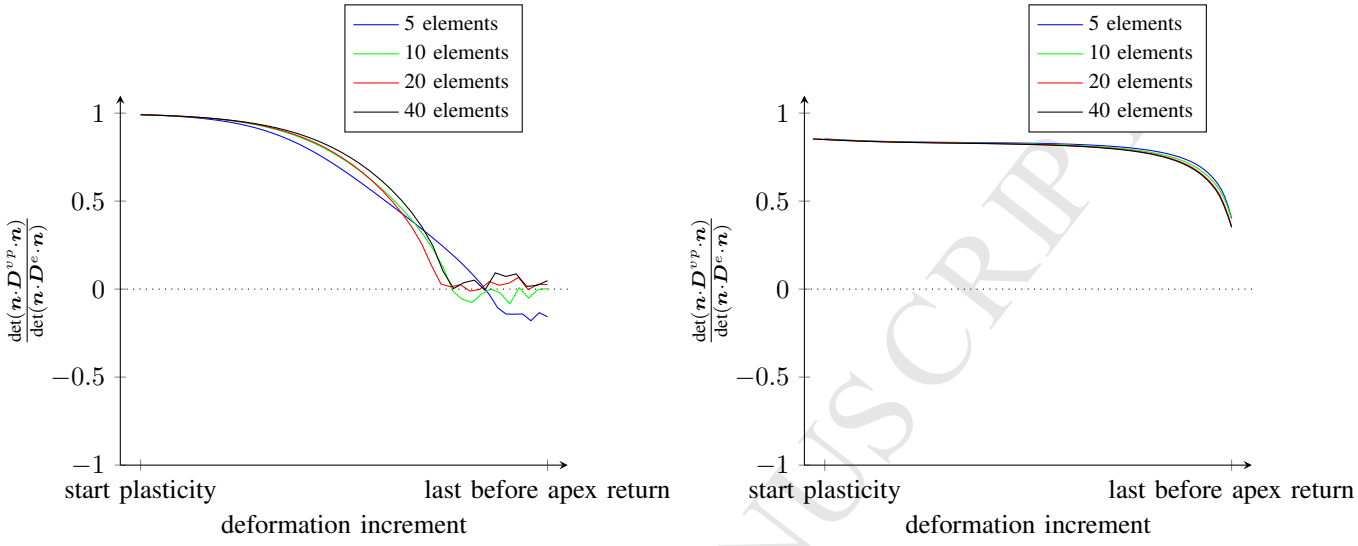

(a) JH2-rd model

(b) JH2-V model

Figure 12: A normalized determinant of the acoustic tensor, computed in a single integration point of the weakest element in the tapered bar test. A negative value indicates a loss of ellipticity of the boundary value problem. This will lead to mesh-dependent results.

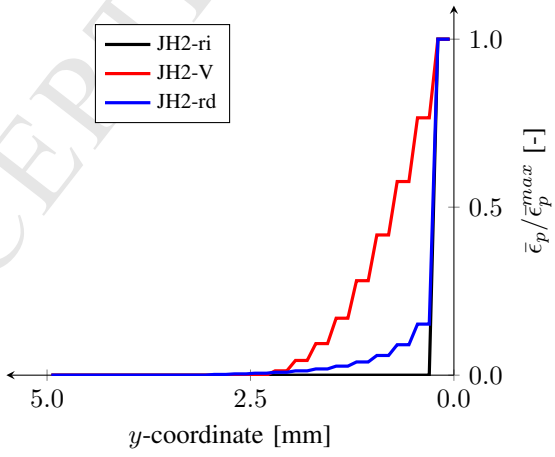

Figure 13: Normalized equivalent plastic strain plotted along the tapered bar, loaded under tension. Results are obtained for the 20 element case with three different material models.

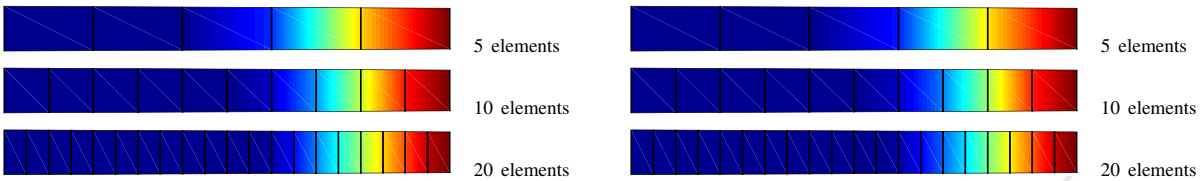

(a) JH2-ri model.

(b) JH2-V model.

Figure 14: Tapered compression bar, equivalent plastic strain plots. Localization upon mesh refinement is absent.

zone rather than to localize in a single element. This behaviour is to be expected since the tapered bar is confined in lateral directions and the material strength increases with pressure. As the bar is loaded the material will experience both plastic softening and an increase in strength with increasing pressure. The latter is observed as an effective hardening of the material. As a result plasticity spreads through the bar. The results for the JH2-V model are similar and can be found in Figure 14b. The similarity was to be expected, as the difference in strength of the JH2-V model is mainly found under tension (Figure 1).

4.2.4. Tapered bar in dynamics

The previous results on the tapered bar were all obtained by performing quasi-static simulations. These exclude inertia effects and wave propagation in the bar. Since the JH2 model was originally designed for dynamic loading the model's behaviour under dynamic loads should also be checked. The test case remains the same tapered bar with an applied displacement. The displacement is applied at a rate of 0.1m/s, similar to the quasi-static tapered bar case. This applied rate or velocity will generate a stress wave in the bar. The stress wave will propagate at approximately 10.000m/s given the material parameters from Table 1. For the current boundary conditions the stress wave will reflect multiple times before failure is initiated in the weak element.

To obtain the dynamic results an implicit time integration scheme is applied. The Newmark-β scheme is used with $\beta = {}^1/_4$ and $\gamma = {}^1/_2$. This solution scheme uses the consistent tangent as well as the mass matrix to iteratively find a converged solution for each load increment.

Figure 15a shows the equivalent plastic strain in the tapered bar under dynamic tensile loading simulated with the JH2-ri model. Localization of the plastic deformation can be observed at the right side of the tapered bar, similar to the quasi-static results shown previously in Figure 9a. The equivalent plastic strain plots are obtained at the final increment before apex return is invoked. Figure 16a shows the results for the tapered bar under dynamic loading with the JH2-V model. As seen before, this model provides regularization and the results are mesh independent.

The load displacement graphs of the dynamic tapered bar test are shown in Figure 15b and 16b. The graphs are similar to the quasi-static case in terms of peak force, but post peak behaviour can be found to differ. For the JH2-ri model the snap-back behaviour is not present in dynamics as arc-length control cannot be applied. For the JH2-V model the total deformation between the peak force and the sudden drop of strength under apex return is extended. In both cases strong oscillations can be found after apex return. This is caused by the sudden loss of strength experienced during apex return. These oscillations may cause additional damage to the material after apex return.

4.2.5. Tapered bar concluded

From the tapered bar tests it is clear that the JH2 model suffers from mesh dependency under tension and shear loading. For compressive loading there is no apparent mesh dependency. The original JH2 model with rate dependency (JH2-rd model) can regularize the problem under shear, but no regularization is found under tension. The proposed JH2-V model offers regularization for both the tensile and shear loaded cases. This conclusion holds for both quasi-static and dynamic loading.

4.3. Mesh Bias

An important problem related to mesh dependency is mesh bias of the results. When studying ceramics a mesh bias can result in an erroneous prediction of crack propagation. As cone cracks can lead to full armour failure in ceramic armour systems it is of vital importance to objectively capture cracks in the simulations. To study the effect

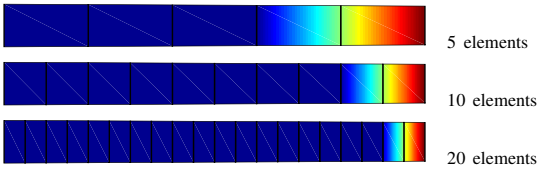

(a) Equivalent plastic strain. Note the localization upon mesh refinement on the right side of the bar.

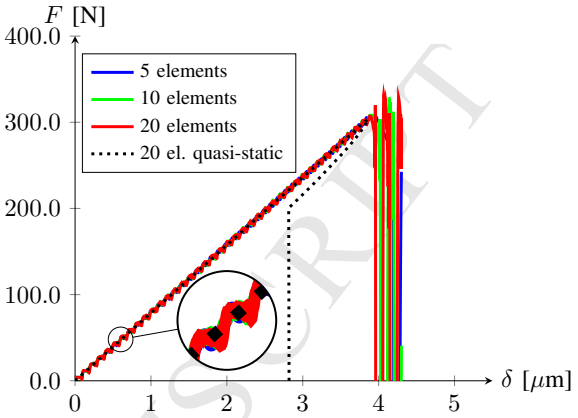

(b) Force displacement graph. All three meshes give the same results. Black dotted line is obtained by quasi-static simulation of the tapered bar under tension.

Figure 15: Tapered tension bar results for the JH2-ri model under dynamic loading.

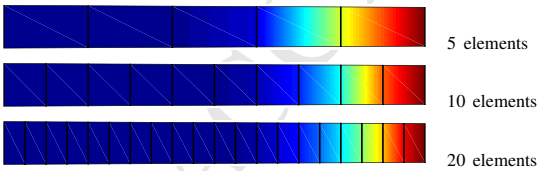

(a) Equivalent plastic strain. Localization upon mesh refinement is absent.

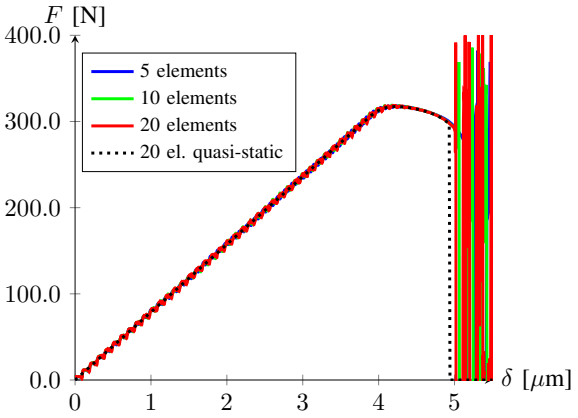

(b) Force displacement graph. All three meshes give the same results. Black dotted line is obtained by quasi-static simulation of the tapered bar under tension.

Figure 16: Tapered tension bar results for the JH2-V model under dynamic loading.

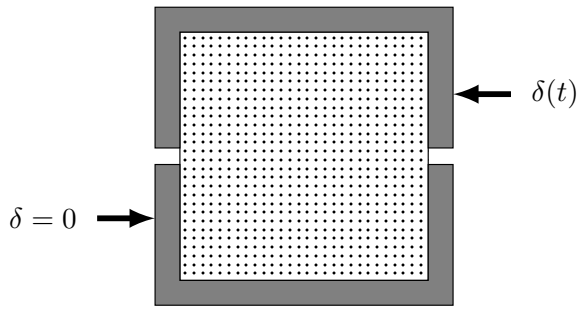

(a) Schematic representation.

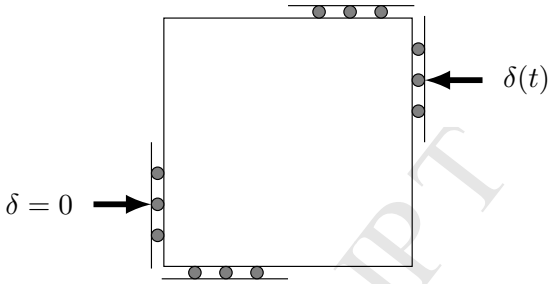

(b) Simulation boundary conditions.

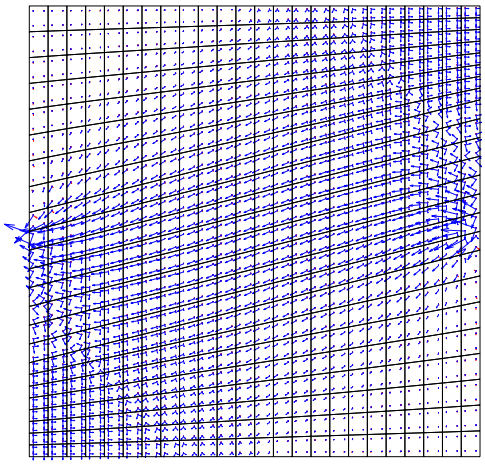

(c) Principal stress direction, elastic loading, upward slanted mesh.

Figure 17: Direct shear test.

of mesh bias in the JH2 model a direct shear test is considered. By varying the mesh alignment the mesh bias effect can be demonstrated.

The direct shear test is commonly applied in rock mechanics to determine a material's shear strength [37]. A schematic representation of the direct shear test is shown in Figure 17a. A cubic specimen is placed in two boxes, each enveloping half of the specimen. The bottom box is fixed, while the top box is displaced to load the specimen in shear. For the current test a loading rate of 1.0 m/s is assumed. The simulations are performed quasi-statically, thus excluding inertia effects. For the current test the width and height of the specimen are assumed to be 3mm.

In the direct shear experiment the boundary conditions of the specimen are defined by the contact with the boxes, which can only transmit compressive loads. For the FE simulations the boundaries are applied as in Figure 17b. The specimen sides are supported in normal direction over half of their length only. These conditions are a simplification of the contact problem defined by the boxes. The current boundary conditions were found to prevent boundary induced tensile damage in the material.

To study the effect of bias three different meshes are used: a horizontally aligned mesh, an upward slanted mesh and a downward slanted mesh. These meshes will be referred to as the mesh with "no bias", "upward bias" and " downward bias". The upward biassed mesh is aligned with the principal stress direction found for this direct shear test, as is shown in Figure 17c.

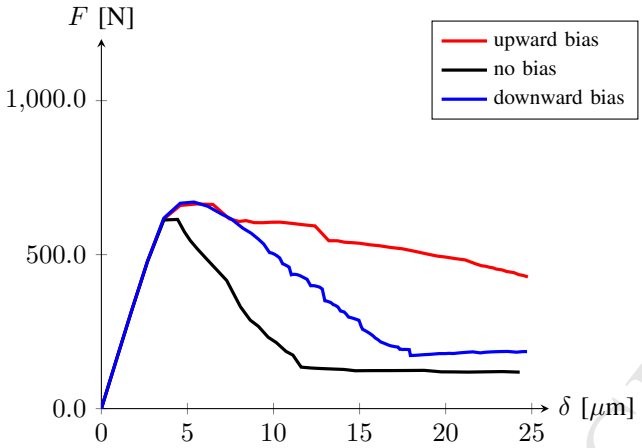

Figure 18: Direct shear test using the JH2-ri model. The peak strength of the material is more or less equal for all meshes. However, a strong mesh dependency can be found in the post peak behaviour of the material.

4.3.1. Direct shear for JH2-ri

To provide a benchmark of the direct shear test initially the JH2-ri model is used. Material parameters are the same as those used to study the tapered bar case, except the Poisson ratio which is $\nu = 0.22$ for the direct shear tests. Load displacement data for the different mesh alignments are shown in Figure 18. Peak forces are similar for all three meshes, while large differences in post peak behaviour can be found. The meshes with an up- and downward bias are able to maintain a higher force in the post-peak regime when compared to the horizontally aligned mesh. Of all three mesh alignments the upward slanted mesh predicts the highest force for a given level of deformation, thus having the most ductile post peak response. These results once again illustrate the mesh dependency problem facing the JH2-ri model. Figure 20a shows the damage profiles of this direct shear test after 25μm of applied deformation. For all three mesh directions the damage profile is found to follow the mesh alignment. This is particularly clear in the upward slanted mesh, where two lines of high damage (i.e. cracks) are found to propagate from the boundary along a single line of elements. These damage profiles clearly demonstrate the mesh bias problem for the JH2-ri model.

4.3.2. Direct shear for JH2-rd

Figure 20b shows the damage variable after 25μm of applied deformation for the JH2-rd material model. The viscosity is the same as for the tapered bar test. The damage profiles for the JH2-ri and JH2-rd models appear to be similar and both show a mesh bias in the results. This is in line with the previous sections, where the JH2-rd model was found to provide insufficient regularization. The load displacement graph for this model can be found in Figure 19. Compared to the JH2-ri model the peak values are considerably higher, for the horizontal aligned mesh the difference is 30.59%. The post peak behaviour for the JH2-rd model does still show mesh dependence. Where the mesh dependence is a consequence of the bias effect and is not related to the mesh size as seen for the tapered bar.

4.3.3. Direct shear for JH2-V

The damage profiles for the JH2-ri model are compared to the JH2-V model in Figure 22. The viscosity is the same as for the tapered bar test. For the horizontally aligned mesh it is clear that damage is also found outside the middle two rows of elements. Similarly the downward slanted mesh predicts failure in a larger zone than what is found for the JH2-ri model. The upward slanted mesh simulated with the JH2-V model shows damage to occur in a smaller zone compared to the JH2-ri model. The damage profiles for all three meshes show more resemblance for the JH2-V model compared to the profiles of the JH2-ri model. It must be stated that although the results are an improvement, there is still some mesh bias present in these results. The load displacement data can be studied from Figure 21. The peak force values are found to increase significantly compared to the JH2-ri model. For the horizontal aligned mesh the difference is as large as 52.77%, much more than what was found for the JH2-rd model. This is the opposite of what was found for the tapered bar test, where JH2-rd predicted a larger peak force than the JH2-V model. For the JH2-V model the post peak behaviour is now found to be similar for all three meshes up to $15-20\mu$m of deformation.

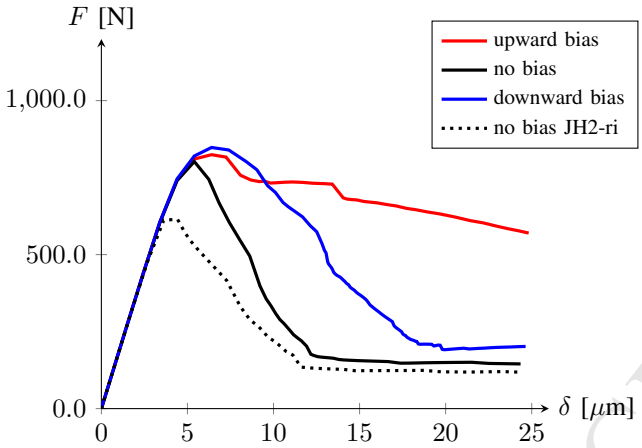

Figure 19: Direct shear test using the JH2-rd model with $C = 0.025$. A strong mesh dependency is present in the post peak behaviour of the material.

4.3.4. Mesh bias reconsidered

The direct shear test has been simulated with four noded quadrilateral elements. These elements are known to suffer from mesh locking. To alleviate mesh locking, the B-bar method developed by Hughes [38] is applied. This method relies on a mixed integration scheme. Deviatoric stresses are integrated using a $2*2$ Gauss integration scheme, while the hydrostatic stress is computed using a reduced 1 point Gauss integration.

Figure 23 shows the load displacement plots for both the JH2-ri and JH2-V models simulated with the B-bar method. The simulation results with the B-bar method appear to be much less mesh dependent, as the post peak responses lie closer for all three meshes. This holds true for both the JH2-ri and JH2-V model.

The damage profiles of the direct shear test with the B-bar method are shown in Figure 24. For the JH2-ri model the profiles are similar for all three meshes. Similarly, the JH2-V model shows good agreement for the damage profiles from all three meshes. For the mesh with horizontal alignment the JH2-ri model predicts failure in a single row of elements. The JH2-V model results in a failure zone including and surrounding this central line of elements. These results show that although mesh bias may be strongly reduced by using the B-Bar method they may still suffer from minor spurious localization.

4.3.5. Mesh bias concluded

The direct shear test has been simulated using the JH2-ri , JH2-rd and JH2-V models. The JH2-ri model showed a clear mesh bias effect in both the damage profile and the load displacement plots. Using the JH2-rd model did not remove or reduce this type of the mesh dependency. This is in line with the results from the previous section where JH2-rd was not able to fully regularize the tapered bar test. When the JH2-V model is applied the damage profiles clearly show a reduced mesh bias effect. This is also confirmed by the load-displacement data. When using the B-bar method with the JH2-V model the mesh bias can be reduced even further, while still predicting a failure zone wider than a single line of elements.

5. Discussion

The proposed viscosity of the JH2-V model has a linear formulation. In the previous sections it was shown that this regularizes the solution of the tapered bar case for all investigated load scenarios. However, these results were all obtained for the same loading rate. If the applied loading rate changes by some orders of magnitude the time scale of the load may be of a different order compared to the relaxation time of the viscous system. This mismatch in load and relaxation time can lead to one of the two following problems. The first problem appears for low loading rates, where the viscosity may be insufficient to provide regularization [39]. For the tapered bar this is easy to show, as localization reappears for very low loading rates. A non-local model may be used in addition to viscoplasticity to solve for this

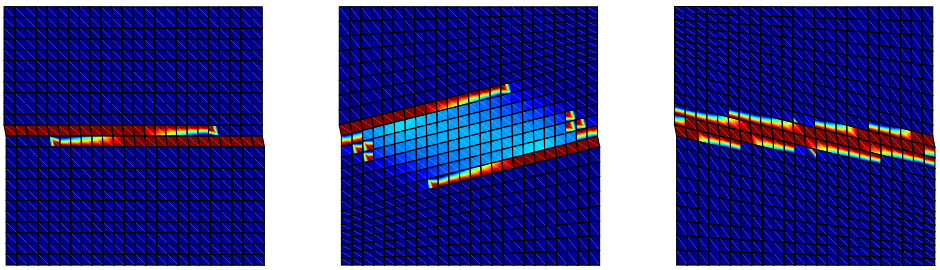

(a) JH2-ri

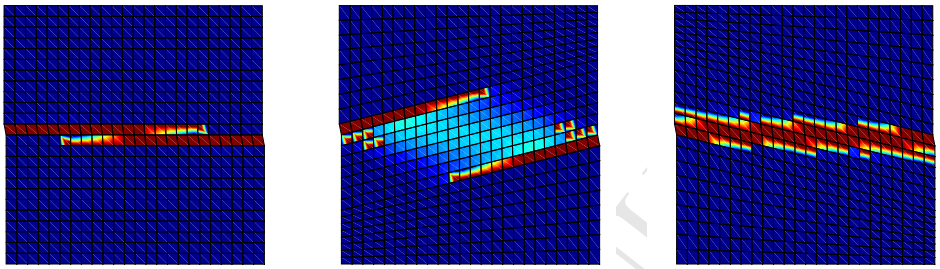

(b) JH2-rd

Figure 20: Direct shear test, damage scalar $D \in [0..1]$ is plotted. Different mesh alignment is considered from left to right.

problem at low loading rates [26]. A second problem for viscous regularization can be found for much larger loading rates, where the failure zone size is found to increase dramatically in size. The latter problem will be addressed in the current section. The loading rate effect is studied for the JH2-V model. The JH2-rd model is not used, as previous results showed unsatisfactory regularization for this model. The tapered bar under tension is considered. The case is simulated dynamically, where a velocity boundary condition is applied to generate a tensile stress wave.

The proposed viscous model has been studied for its regularizing properties up to this point. The current section will end by showing the physical implications of the proposed viscous model. To do so, a spall experiment is simulated and results are compared.

5.1. Loading rate

Figure 25a shows the equivalent plastic strain profiles for the tapered tensile bar subjected to a range of loading rates. The profiles are plotted right before apex return is invoked in the weak element. From top to bottom the applied loading rate is 0.05, 0.1, 0.2, 0.4, 0.8, 1.6, 3.2, 6.4 m/s. Note that the applied loading rate has been 0.1 m/s so far.

It can be seen that the lower loading rate of 0.05m/s predicts a smaller failure zone. If the failure zone size falls below the element size the results would be similar to those obtained by the standard JH2-ri model. Please note that the regularization effect is still present and would reappear upon mesh refinement. For increased loading rates these figures clearly demonstrate a widening of the failure zone. For the four highest loading rates plastic deformation can even be found to spread through the entire bar. The equivalent plastic strain profile found in Figure 25b confirms the widening of the failure zone with increased rate.

5.2. Non-linear viscosity

In the previous section the failure zone size was found to increase rapidly with loading rate. Figure 25b shows that an increase of loading rate from 0.1 to 0.4m/s is sufficient to double the failure zone size from 2.5 to 5.0mm. When applying the JH2-V material model for real world problems (e.g. indentation or impact simulations) the loading rates may differ by a few orders of magnitude. An increase of failure zone size of this magnitude may not be desired. For regularization this increase is unnecessary and physically it may be unrealistic. To limit the failure zone size for high

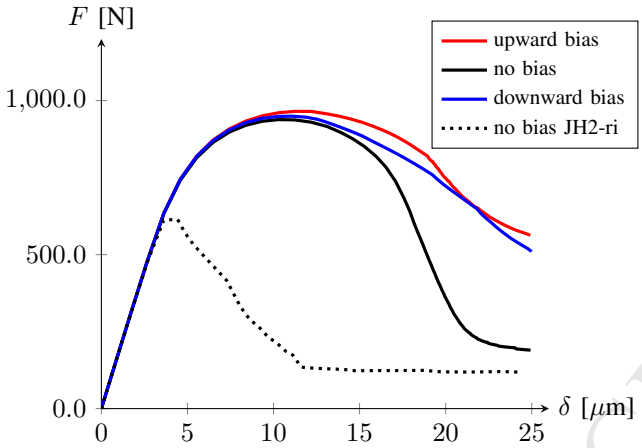

Figure 21: Direct shear test using JH2-V model with $\eta = 0.2 \cdot 10^{-3}$ GPa·s. The peak shear force is similar for all meshes. Compared to the JH2-ri model results there is a large increase in peak force. The post peak behaviour is similar for all three meshes, up to a deformation of around 15μm.

rates the viscosity parameter must be reduced. The simplest way to do this is manually through the input parameters. The viscosity would be problem dependent and would require prior knowledge on the occurring rates in the material during the simulation. A second and more robust approach would be to use a non-linear viscosity formulation, in which the viscosity is automatically reduced as the loading rate increases. The second option is chosen and the original viscosity formulation from (14) is reformulated. For low loading rates the original model is used, but beyond a threshold rate of $\dot{\lambda}_t$ a logarithmic function is be used. The apex pressure may be formulated to read

$$T(\dot{\lambda}) = \begin{cases} T_0 + \eta\dot{\lambda} & \text{for } \dot{\lambda} < \dot{\lambda}_t, \\ T_t\left(1 + \frac{\eta\dot{\lambda}_t}{T_t}\ln\left(\frac{\dot{\lambda}}{\dot{\lambda}_t}\right)\right) & \text{else.} \end{cases} \tag{26}$$

The apex pressure corresponding to the threshold rate can be found as $T_t = T_0 + \eta\dot{\lambda}_t$. The formulation in (26) is C^1 continuous, which aids in the convergence of the local Newton-Raphson scheme. Also note that this formulation converges to the linear viscosity formulation (14) for $\dot{\lambda}_t \to \infty$.

Figure 26 shows how the apex pressure from (26) evolves with rate in the mixed linear/logarithmic formulation. A viscosity $\eta = 0.2 \cdot 10^{-3}$ GPa·s and an initial apex pressure $T_0 = 0.2$ GPa are used. The black dotted line provides the evolution of the apex pressure in the limit case of a viscosity formulation with $\dot{\lambda} = \infty$, the black dashed line is the fixed apex pressure found for the JH2-ri and JH2-rd models. The coloured lines show the evolution of the apex pressure for a variation of the threshold rate $\dot{\lambda}_t$. The increase of apex pressure (i.e. strength) with loading rate for rates above the threshold value is considered. As the rate increases the incremental increase in strength gradually reduces. For sufficiently high rates the increase in material strength may even become negligible and approaches zero. If the strength increase with loading rate is sufficiently small the material model effectively loses its rate dependency and thus loses its regularizing property. This effect can be found for sufficiently large loading rates. How large this loading rate should be before the regularization is lost depends on the threshold value. For a lower threshold value a smaller rate will suffice to lose the capability of regularization.

The apex formulation (26) is used to simulate the tapered bar for loading rates ranging from 0.05 – 6.40m/s. The following results are found for $\eta = 0.2 \cdot 10^{-3}$ GPa·s and three threshold values $\dot{\lambda}_t = 5.0,\ 50.0$ and $500.0\ \text{s}^{-1}$. Figure 27 shows the equivalent plastic strain profiles along the bar axis, plotted for three different threshold values $\dot{\lambda}_t$. On top in Figure 27a a low value of the threshold $\dot{\lambda}_t = 5.0\ \text{s}^{-1}$ is used. All loading rates show that most failure occurs in the weak element of the bar. These results appear to be similar to the inviscid model results and one could conclude that this threshold value does not provide sufficient regularization. This is in line with previous observations from Figure 26, where it was concluded that regularization may be lost if the rate is relatively high compared to the threshold value.

For a threshold value $\dot{\lambda}_t = 50.0\ \text{s}^{-1}$ the failure can already be found to spread over a zone rather than to occur in a single element, as is shown in Figure 27b. For this threshold value all loading rates produce similar failure zones at

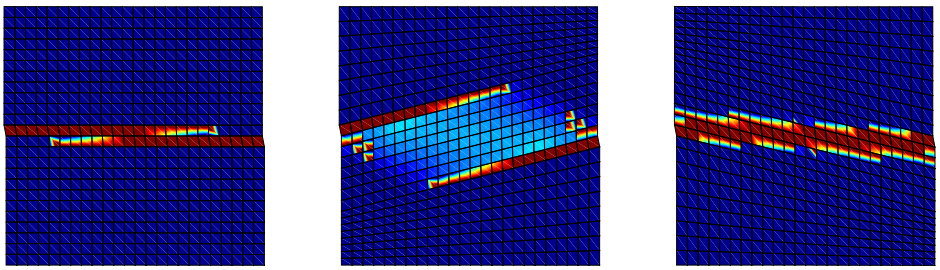

(a) JH2-ri

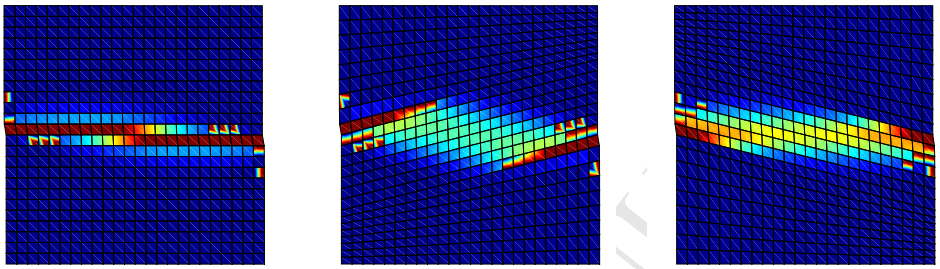

(b) JH2-V

Figure 22: Direct shear test, damage scalar $D \in [0..1]$ is plotted. Different mesh alignment is considered from left to right.

the weak side of the bar. Small deviations in peak values are observed, but the main profile shapes are maintained. For this threshold value it appears that the spreading of the failure zone is limited for increasing values of loading rate.

When the threshold value is increased to $\dot{\lambda}_t = 500.0\ \mathrm{s}^{-1}$ the profiles of Figure 27c are found. These show a growing failure zone size with loading rate. As a comparison the results for the limit case of a viscosity with $\dot{\lambda} = \infty$ are added as the dotted lines. Up to a rate of 0.80m/s both parameter sets give the same results and the solid and dotted line are on top of each other. Only for higher rates there is a noticeable difference in the results. For the finite threshold rate $\dot{\lambda}_t = 500.0\ \mathrm{s}^{-1}$ the equivalent plastic strain profiles for 3.20 and 6.40m/s are found to approach one another. This shows that the desired limiting behaviour of the mixed linear/logarithmic viscosity formulation remains present, but only for a high loading rate. In practice the latter means that the failure zone size is not only controlled by the viscosity η but also through the threshold rate value $\dot{\lambda}_t$.

The tapered bar problem simulated with three values of the threshold rate shows that the failure zone size can be limited by the linear/logarithmic formulation. It does depend on the chosen value of the threshold, if chosen too small the model loses its regularizing properties, if chosen too high the failure zone size may be larger than desired.

The newly proposed mixed linear/logarithmic formulation is subjected to a mesh refinement study. Figure 28 shows the resulting equivalent plastic strain profiles for four different meshes, loaded with a suddenly applied velocity of 0.8m/s. The profiles are found to converge for a increasingly fine mesh. It is therefore concluded that the mixed linear/logarithmic formulation can provide mesh independent results. However, the limitations on the threshold rate mentioned in the previous paragraph should be taken into account.

A final remark on the viscosity formulation is given. In section 4 it was concluded that the JH2-V model with a linear apex viscosity is sufficient for regularization. In the current section it is shown that this also holds for a mixed linear/logarithmic formulation. The latter is a more general formulation as it can be shown that the linear/logarithmic formulation reduces to a linear one for $\dot{\lambda} \to \infty$. The mixed formulation is preferred, as it allows for control of the failure zone size. Which may be required from a physical point of view. Obtaining an objective and physical response of the proposed linear/logarithmic formulation now depends on the model parameters η and $\dot{\lambda}_t$. For a given type of ceramic these parameters will have to be calibrated to match experimental results. The next section shows how this can be done for an alumina ceramic.

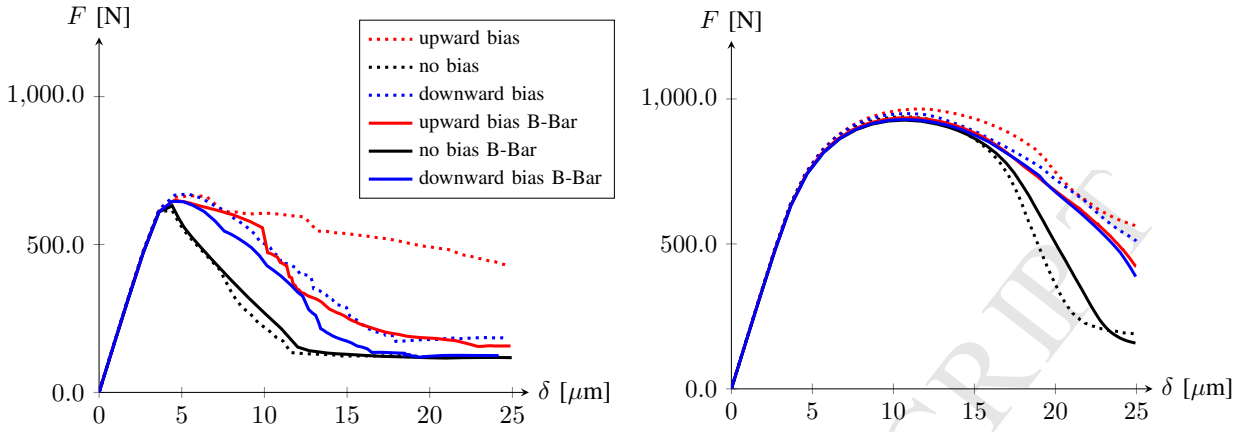

(a) JH2-ri model.

(b) JH2-V model.

Figure 23: Direct shear test load displacement plots. Solid lines are obtained with the B-bar method, dotted lines without.

5.3. *Comparison to experiments*

Until now the proposed viscous model has been studied for its numerical behaviour only. The previous sections have shown that the proposed model can lead to mesh-independent results. As a final step the physical implication of the proposed model is investigated. A spall experiment on alumina ceramic is used, as described in [32]. In this experiment an alumina plate is subjected to a stress wave, propagating though the thickness of the plate. The centre of this plate experiences uniaxial strain conditions. Therefore the test is simulated as a single column of elements, where only axial movement is allowed. A compressive stress pulse is induced by applying one of the velocity profiles from Figure 29a to the bottom surface of the column. These profiles are simplified representations of the waves shown in [32]. In the current paper nine different wave amplitudes are considered, for each a spall strength and a certain loading rate can be determined. Upon reflection of the compressive stress wave at the (free) top surface of the column tensile stresses will be generated and the material fails. The paper [32] provides the material properties $E = 360$GPa, $\nu = 0.22$ and $\rho = 3890$ kg/m^3. The other model parameters are taken from Table 1, but with $P_{HEL} = 3.5$ GPa, $\sigma_{HEL} = 4.125$ GPa, $d_1 = 0.005$ and $d_2 = 0.75$. A minimal failure strain of $\bar{\epsilon}_p^{max} = 1.5 \cdot 10^{-4}$ is enforced to prevent immediate full failure below the static apex pressure T.

For the spall simulation the strength is defined as the highest axial stress found in all material points, up to the point of first apex failure. At the same location and time where this highest stress is found, the strain rate will also be determined. This strain rate is simply defined as the rate of total axial strain.

Figure 29b shows the predicted spall strength from the simulations, compared to the experiment. It is clear that the JH2-ri and JH2-rd models fail to capture the rate dependency of the spall strength. The JH2-ri model predicts a constant strength as a function of rate. This agrees well with the theoretical strength of the rate independent JH2 model. This theoretical strength may be computed from the yield surface, as it is the location where the surface is first reached under the applied loading and boundary conditions. For the given material parameters it can easily be shown that this occurs for an axial tensile stress $\sigma = 321.56$MPa. The spall strength predicted by the JH2-rd model is higher than the JH2-ri strength, which can be attributed to the rate dependency in the model. The strength for the JH2-rd model is nearly constant, a slight increase with loading rate may be observed. For the higher rates a minor scatter in the spall strength is found, this can be attributed to the time step size in the simulations. The JH2-V model does capture the rate dependency, a good fit is found for $\eta = 0.028 \cdot 10^{-3}$ GPa·s and $\dot{\lambda}_t = \infty$. The results for finite values of the threshold rate are also shown in Figure 29b, they do not match the experimental results for the chosen values of η and $\dot{\lambda}_t$.

With the spall strength results the threshold rate $\dot{\lambda}_t$ can also be given a physical meaning. Figure 29b shows a change in slope of the spall strength at the finite threshold rates $\dot{\lambda}_t$. Physically this change in slope can be related to a change in failure mechanism, which is often observed when investigating rate dependency of brittle materials. If known, one may use the rate at which the mechanism changes as the value of $\dot{\lambda}_t$.

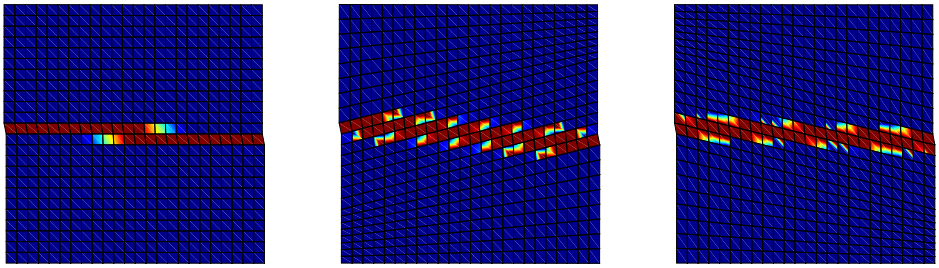

(a) JH2-ri

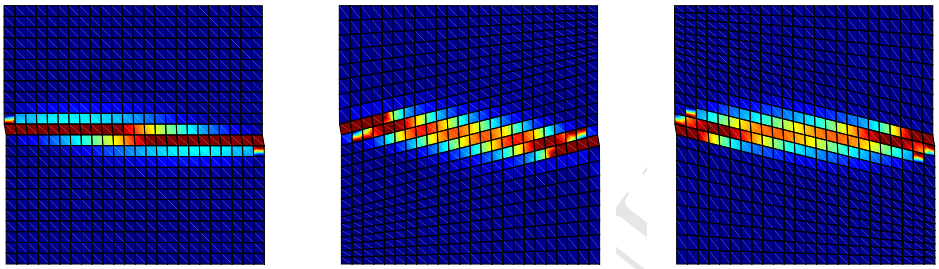

(b) JH2-V

Figure 24: Direct shear test using JH2-ri model (top) and JH2-V model with $\eta = 0.2 \cdot 10^{-3}$ GPa·s (bottom). Damage scalar $D \in [0..1]$ is plotted. Different mesh alignment is considered in the three figures. A mixed integration scheme is used for all simulations.

When only the spall strength is considered it is clear that a finite threshold rate is not required to match the experimental data. In subsection 5.2 it was concluded that an unphysical failure zone size is a reason to use a finite threshold rate. Therefore a check on the failure zone size is performed for the spall test, to confirm that the current infinite threshold rate is indeed correct. The simulations are now extended to a 2d simulation on a 10mm high and 2.5mm wide plane strain column. Boundary conditions and material parameters remain the same as before.

In Figure 30 the failure zones from the spall simulations are compared to the experimental result. Experimentally the spall zone could only be studied for the lowest applied stress wave, as for higher stress waves the specimen could not be recovered. For the original experimental results a failure zone size of 2.3mm is reported, starting 2.1mm from the free surface. The simulation results are obtained by applying wave 2 from Figure 29a to the structure , with the same material parameters as those used to obtain the spall strengths of Figure 29b. The colours in Figure 30 represent the damage variable $D \in [0..1]$. The JH2-rd results are omitted, as this model already failed to capture the spall strength. The JH2-V and JH2-ri results are both presented, the JH2-ri model is added because it is a limit case of the JH2-V model (i.e. $\eta \to 0$). All simulation results show full failure in the 2.3mm zone, similar to the experiment. The JH2-ri model shows either full damage or no damage in the mesh, which once again confirms the results for the JH2-ri model being mesh dependent. The JH2-V model results show a more gradual failure process, with material which is neither intact nor fully failed. The zone with partial failure extends beyond the 2.3mm wide zone. It is uncertain if this is also true in the experiments, as only macrocracks (i.e. full failures) are visible. As more experimental data become available this question might be answered. For now the JH2-V model with $\eta = 0.028 \cdot 10^{-3}$ GPa·s and $\dot{\lambda}_t = \infty$ is considered to be sufficient, as the spall strength agrees with the experimental data and a comparison with the single available experimentally measured failure zone size does not offer any objection to this conclusion. More experimental results on the failure zone are required to validate this choice.

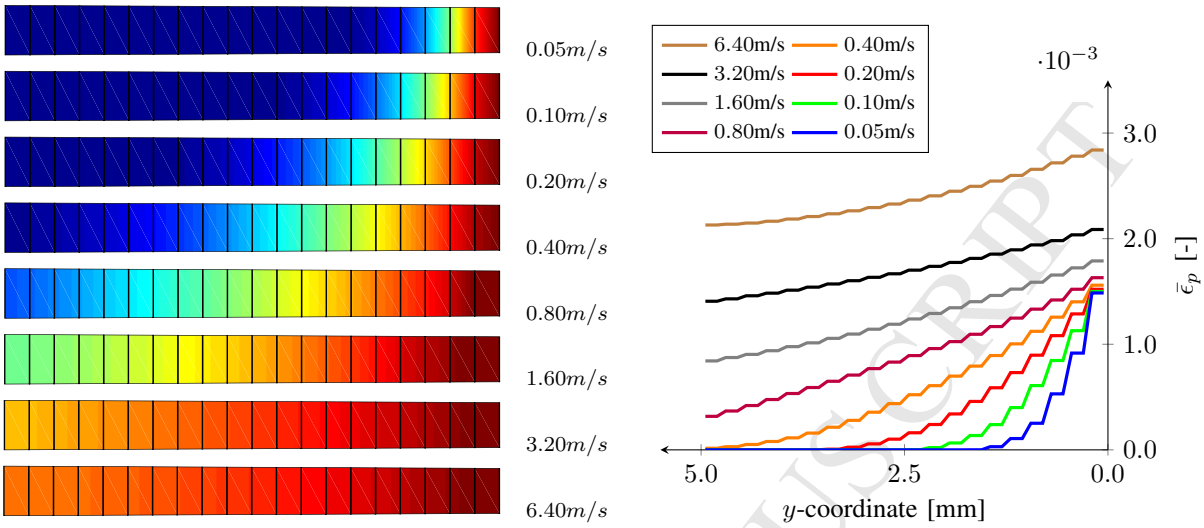

(a) Equivalent plastic strain.

(b) Equivalent plastic strain profile along the tapered bar axis.

Figure 25: Tapered tension bar results for the JH2-V model with a linear rate dependency. The velocity is applied suddenly on the boundary.

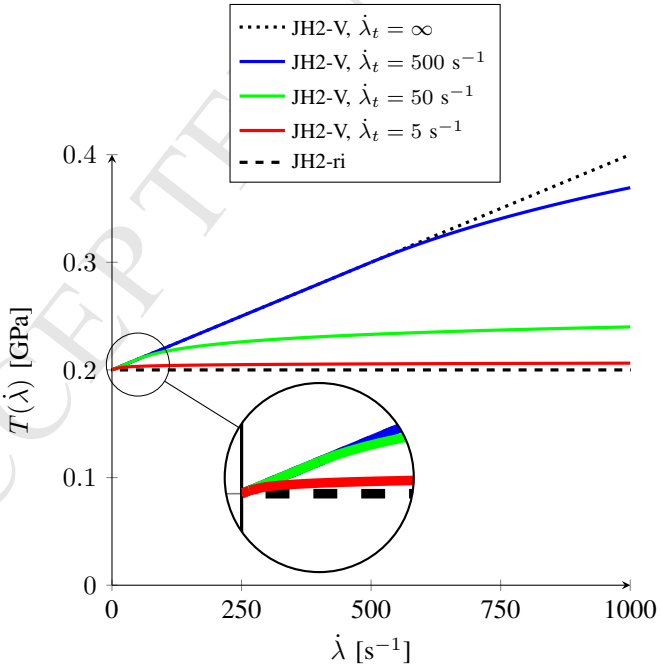

Figure 26: Apex pressure T from (26) plotted as a function of loading rate. Three different threshold rates $\dot{\lambda}_t$ are used. The apex evolution for JH2-V and JH2-ri with rate are added as a reference.

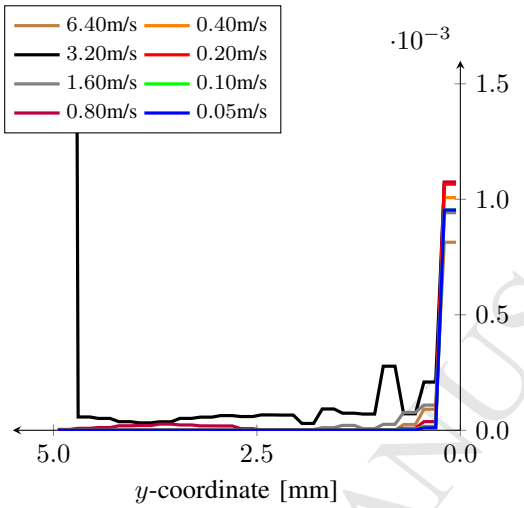

(a) JH2-V model with linear/logarithmic formulation and $\dot{\lambda}_t = 5.0\,\mathrm{s}^{-1}$.

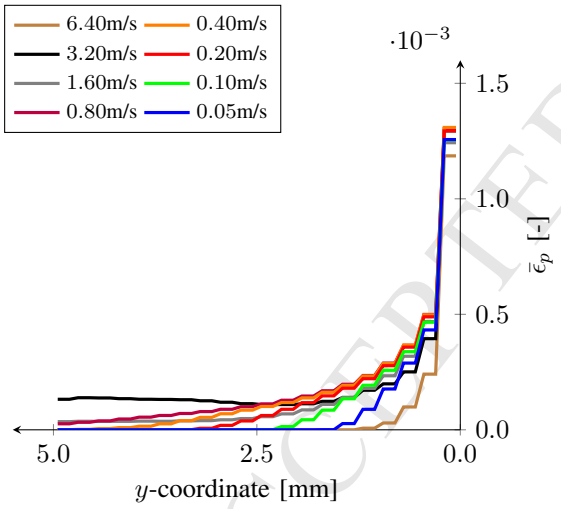

(b) JH2-V model with linear/logarithmic formulation and $\dot{\lambda}_t = 50.0\,\mathrm{s}^{-1}$.

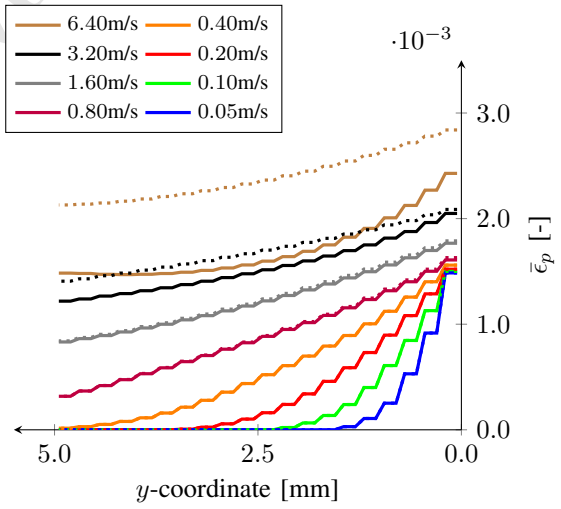

(c) JH2-V model with linear/logarithmic formulation and $\dot{\lambda}_t = 500.0\,\mathrm{s}^{-1}$.

Figure 27: Tapered tension bar results for the JH2-V model with a mixed linear/logarithmic rate dependency. Equivalent plastic strain profiles are plotted along the bar axis.

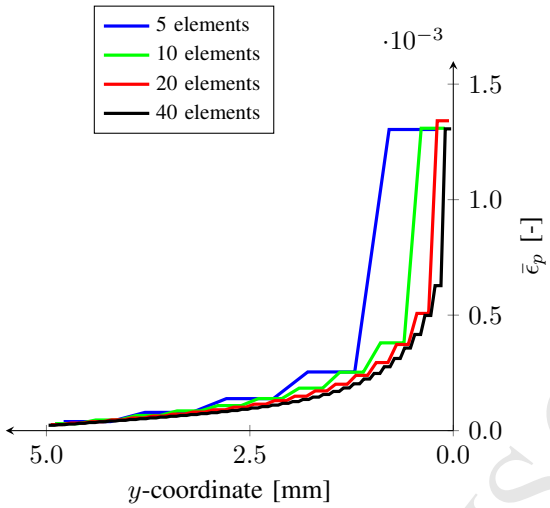

Figure 28: Tapered tension bar results for the JH2-V model with a mixed linear/logarithmic rate dependency. Threshold parameter $\dot{\lambda}_t = 50.0\ \mathrm{s}^{-1}$. Equivalent plastic strain profiles are plotted along the bar axis for four different meshes.

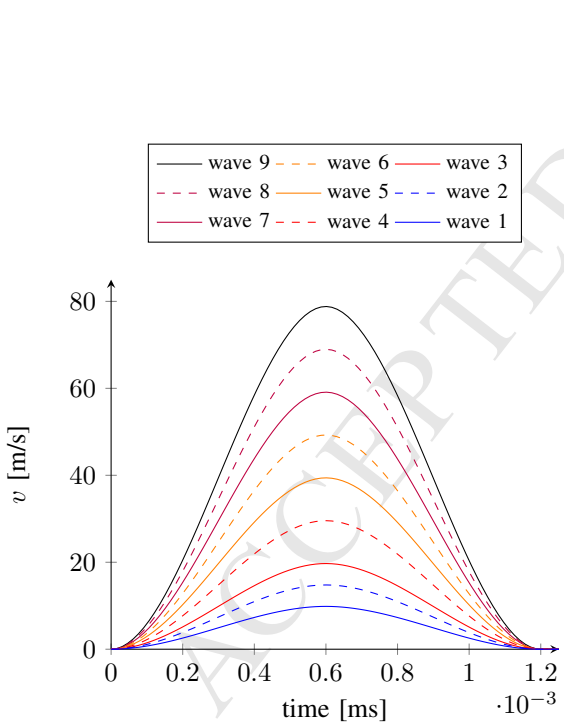

(a) Applied velocity to induce a stress wave in the spall simulations.

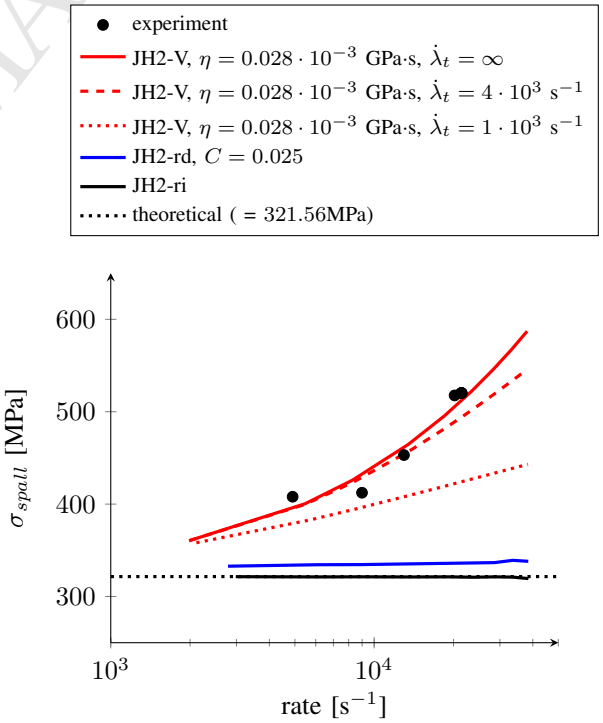

(b) Spall strength, experimentally measured and predicted by simulation. The original JH2 model is unable to capture the rate dependency, while the proposed JH2-V model can capture the rate dependency.

Figure 29: Spall test on alumina ceramic, comparing experiments to simulations.

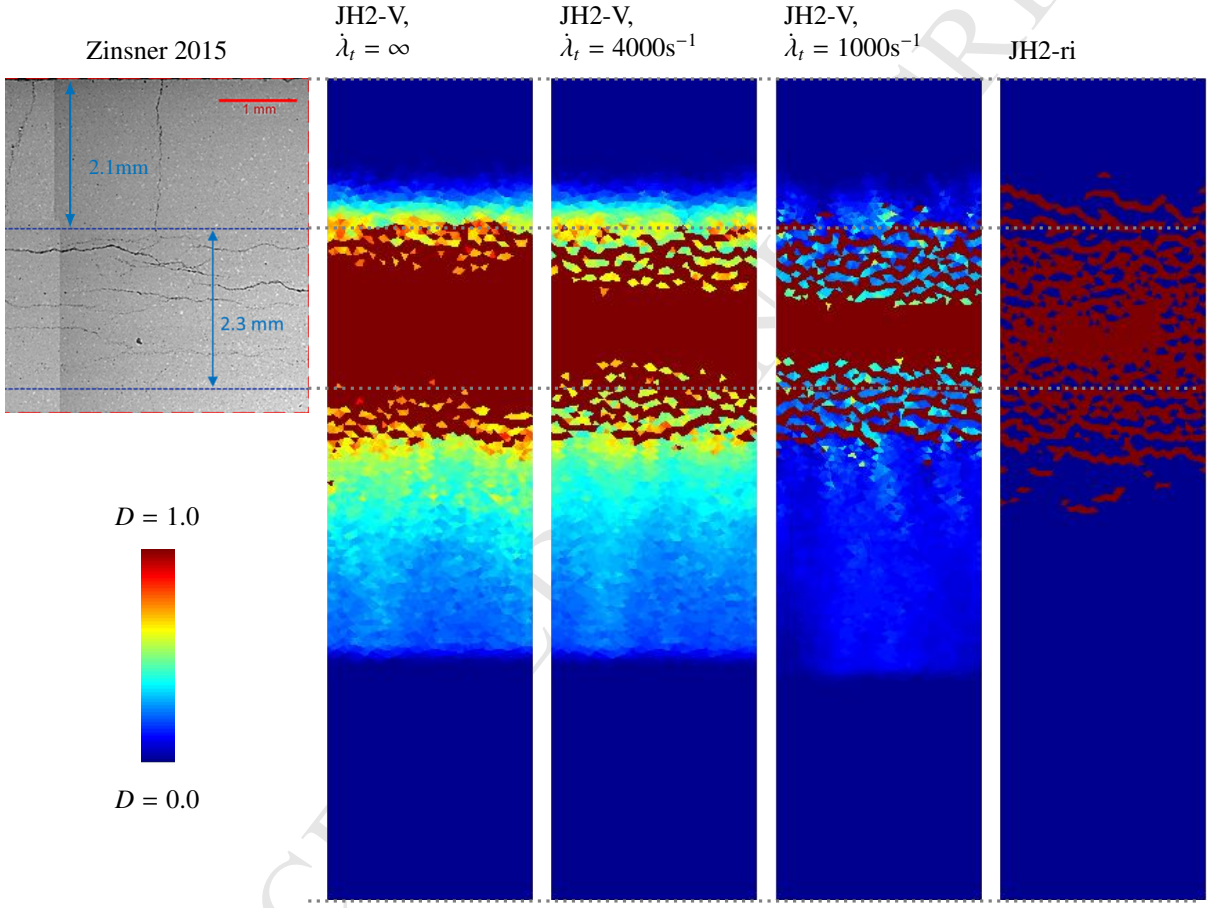

Figure 30: Spall failure zones in experiment (from [32]) and simulations compared. Simulation results show the damage variable $D \in [0..1]$. The JH2-V model results are obtained with $\eta = 0.028 \cdot 10^{-3}$ GPa·s and varying values of the threshold rate $\dot{\lambda}_t$.

6. Conclusions

The JH2 material model was found to suffer from mesh dependency. Tapered bar and direct shear tests showed spurious localization as well as mesh bias. The logarithmic rate dependency included in the original model was found to remove mesh dependency in the tapered bar test under shear loading. However, when using the same model parameters under tensile loading mesh dependency reappeared. In the direct shear test the original rate dependency also failed to provide sufficient regularization.

An apex viscosity was proposed as a modification to the JH2 material model. A linear apex viscosity formulation was found to provide sufficient regularization as spurious localization was not present and mesh bias effects were reduced compared to the JH2 model.

In dynamic simulations the introduced linear formulation revealed a potential problem. When exposed to loading rates ranging over multiple orders of magnitude the predicted failure zone is found to grow fast. In reality a failure zone may not grow as fast, or not at all if the loading rate is increased. To control the failure zone size a combined linear/logarithmic viscosity formulation was proposed. The combined linear/logarithmic apex viscosity was found to limit the failure zone size for higher loading rates while still providing mesh independent results for the range of loading rates considered here. The linear viscosity formulation is found to be a limit case of the mixed linear/logarithmic formulation. Hence the mixed linear/logarithmic formulation is recommended for general use.

As a final step the physical implication of the proposed rate dependent apex pressure was tested by simulating a spall experiment on alumina ceramic. The apex viscosity was found to correctly capture the rate dependent spall strength of the ceramic. The original JH2 material model failed to capture this rate dependency.

References

[1] P. J. Hazell, Ceramic Armour: Design and Defeat Mechanisms, Argos Press, Canberra, 2006.

[2] S. M. Walley, Historical review of high strain rate and shock properties of ceramics relevant to their application in armour, Advances in Applied Ceramics 109 (8) (2010) 446–466. doi:10.1179/174367609X422180.

[3] Z. Rosenberg, E. Dekel, Terminal ballistics, 2nd Edition, Springer, Heidelberg, 2012. doi:10.1007/978-981-10-0395-0.

[4] T. J. Holmquist, G. R. Johnson, The failed strength of ceramics subjected to high-velocity impact, Journal of Applied Physics 104 (2008). doi:10.1063/1.2955456.

[5] D. Sherman, T. Ben-Shushan, Quasi-static impact damage in confined ceramic tiles, International Journal of Impact Engineering 21 (4) (1998) 245–265. doi:10.1016/S0734-743X(97)00063-8.

[6] G. Subhash, S. Maiti, P. H. Geubelle, D. Ghosh, Recent Advances in Dynamic Indentation Fracture, Impact Damage and Fragmentation of Ceramics, Journal of the American Ceramic Society 91 (9) (2008) 2777–2791. doi:10.1111/j.1551-2916.2008.02624.x.

[7] A. A. Wereszczak, T. P. Kirkland, K. T. Strong, T. J. Holmquist, D. S. A, ORNL Quasi-Static Mechanical Characterization and Analysis : FY09 Annual Report to TARDEC Under contract DE-AC05-00OR22725, 2009.

[8] B. G. Compton, E. A. Gamble, F. W. Zok, Failure initiation during impact of metal spheres onto ceramic targets, International Journal of Impact Engineering 55 (2013) 11–23. doi:10.1016/j.ijimpeng.2012.12.002.

[9] J. Wade, S. Robertson, H. Wu, Plastic deformation of polycrystalline alumina introduced by scaled-down drop-weight impacts, Materials Letters 175 (2016) 143–147. doi:10.1016/j.matlet.2016.04.023.

[10] K. A. Iyer, Relationships between multiaxial stress states and internal fracture patterns in sphere-impacted silicon carbide, International Journal of Fracture 146 (1-2) (2007) 1–18. doi:10.1007/s10704-007-9108-z.

[11] T. J. Holmquist, A. A. Wereszczak, Using Hertzian Indentation to Understand the Strength and Ballistic Resistance of Silicon Carbide, International Journal of Applied Ceramic Technology 7 (5) (2010) 625–634. doi:10.1111/j.1744-7402.2010.02540.x.

[12] J. Wade, S. Ghosh, P. Claydon, H. Wu, Contact damage of silicon carbide ceramics with different grain structures measured by Hertzian and Vickers indentation, Journal of the European Ceramic Society 35 (6) (2015) 1725–1736. doi:10.1016/j.jeurceramsoc.2014.12.030.

[13] K. P. Marimuthu, F. Rickhey, J. H. Lee, H. Lee, Spherical indentation for brittle fracture toughness evaluation by considering kinked-cone-crack, Journal of the European Ceramic Society 37 (1) (2016) 381–391. doi:10.1016/j.jeurceramsoc.2016.08.014.

[14] G. R. Johnson, T. J. Holmquist, A computational constitutive model for brittle materials subjected to large strains, high strain rates, and high pressures, Shock Wave and High-Strain-Rate Phenomena in Materials.

[15] G. R. Johnson, T. J. Holmquist, An improved computational constitutive model for brittle materials, AIP Conference Proceedings 309 (1994) 981–984. doi:10.1063/1.46199.

[16] G. R. Johnson, T. J. Holmquist, S. R. Beissel, Response of aluminum nitride (including a phase change) to large strains, high strain rates, and high pressures, Journal of Applied Physics 94 (3) (2003) 1639. doi:10.1063/1.1589177.

[17] C. M. Simha, S. Bless, A. Bedford, Computational modeling of the penetration response of a high-purity ceramic, International Journal of Impact Engineering 27 (1) (2002) 65 – 86. doi:10.1016/S0734-743X(01)00036-7.

[18] A. Rajendran, High Strain Rate Behavior of Metals Ceramics, and Concrete, Tech. rep., University of Dayton Research Institute, Dayton, Ohio (1992).

[19] Q. Zuo, F. Addessio, J. Dienes, M. Lewis, A rate-dependent damage model for brittle materials based on the dominant crack, International Journal of Solids and Structures 43 (11-12) (2006) 3350–3380. doi:10.1016/j.ijsolstr.2005.06.083.

[20] V. Deshpande, A. Evans, Inelastic deformation and energy dissipation in ceramics: A mechanism-based constitutive model, Journal of the Mechanics and Physics of Solids 56 (10) (2008) 3077–3100. doi:10.1016/j.jmps.2008.05.002.

[21] V. S. Deshpande, E. A. N. Gamble, B. G. Compton, R. M. McMeeking, A. G. Evans, F. W. Zok, A Constitutive Description of the Inelastic Response of Ceramics, Journal of the American Ceramic Society 94 (2011) s204–s214. doi:10.1111/j.1551-2916.2011.04516.x.

[22] Z. P. Bazant, F.-B. Lin, Non-local yield limit degradation, International Journal for Numerical Methods in Engineering 26 (8) (1988) 1805–1823. doi:10.1002/nme.1620260809.

[23] N. Fleck, J. Hutchinson, Strain Gradient Plasticity (1997). doi:10.1016/S0065-2156(08)70388-0.

[24] A. Needleman, Material rate dependence and mesh sensitivity in localization problems, Computer Methods in Applied Mechanics and Engineering 67 (1) (1988) 69–85. doi:10.1016/0045-7825(88)90069-2.

[25] A. Winnicki, C. J. Pearce, N. Bićanić, Viscoplastic Hoffman consistency model for concrete, Computers and Structures 79 (1) (2001) 7–19. doi:10.1016/S0045-7949(00)00110-3.

[26] M. Lazari, L. Sanavia, B. Schrefler, Local and non-local elasto-viscoplasticity in strain localization analysis of multiphase geomaterials, International Journal for Numerical and Analytical Methods in Geomechanics 39 (14) (2015) 1570–1592, nAG-15-0036. doi:10.1002/nag.2408.

[27] P. Perzyna, Fundamental problems in viscoplasticity, Advances in Applied Mechanics 9 (1966) 243–377. doi:10.1016/S0065-2156(08)70009-7.

[28] G. Duvaut, J.-L. Lions, inequations en mecanique et en physique [Les].

[29] W. Wang, L. Sluys, R. De Borst, Viscoplasticity for instabilities due to strain softening and strain-rate softening, International Journal for Numerical Methods in Engineering 40 (20) (1997) 3839–3864.

[30] J. C. Simo, J. G. Kennedy, S. Govindjee, Non-smooth multisurface plasticity and viscoplasticity. Loading/unloading conditions and numerical algorithms, International Journal for Numerical Methods in Engineering 26 (10) (1988) 2161–2185. doi:10.1002/nme.1620261003.

[31] Dynaflow Research Group, Jem-jive.
URL http://jem-jive.com

[32] J. L. Zinszner, B. Erzar, P. Forquin, E. Buzaud, Dynamic fragmentation of an alumina ceramic subjected to shockless spalling: An experimental and numerical study, Journal of the Mechanics and Physics of Solids 85 (2015) 112–127. doi:10.1016/j.jmps.2015.08.014.
URL http://dx.doi.org/10.1016/j.jmps.2015.08.014

[33] J.-L. Zinszner, B. Erzar, P. Forquin, Strain rate sensitivity of the tensile strength of two silicon carbides: experimental evidence and mi-

cromechanical modelling, Philosophical Transactions of the Royal Society of London A: Mathematical, Physical and Engineering Sciences 375 (2085). doi:10.1098/rsta.2016.0167.

[34] E. C. Simons, J. Weerheijm, L. J. Sluys, Fully Implicit Plasticity Model for the Characterization of Ceramics in Ballistic Protection, in: P. Forquin, D. Saletti (Eds.), DYMAT, 22nd Technical Meeting: Experimental Testing and Modelling of Brittle Materials at High Strain-Rates, Grenoble, 2016, pp. 17–22.

[35] M. A. Crisfield, Non-Linear Finite Element Analysis of Solids and Structures: Essentials, John Wiley & Sons, Inc., New York, NY, USA, 1991.

[36] M. Jirásek, Mathematical analysis of strain localization, Revue française de génie civil 11 (2007) 977–991. doi:10.1080/17747120.2007.9692973.

[37] Standard Test Method for Performing Laboratory Direct Shear Strength Tests of Rock Specimens Under Constant Normal Force, Tech. Rep. D5607-02, International, ASTM (2002). doi:10.1520/D5607-02.

[38] T. J. Hughes, Generalization of Selective Integration Procedures to Anisotropic and Nonlinear Media, Short Communications (October 1979) (1980) 1413–1418.

[39] Z. P. Bažant, M. Jirásek, Nonlocal Integral Formulations of Plasticity and Damage: Survey of Progress, Journal of Engineering Mechanics 128 (11) (2002) 1119–1149. doi:10.1061/(ASCE)0733-9399(2002)128:11(1119).

original JH2 model

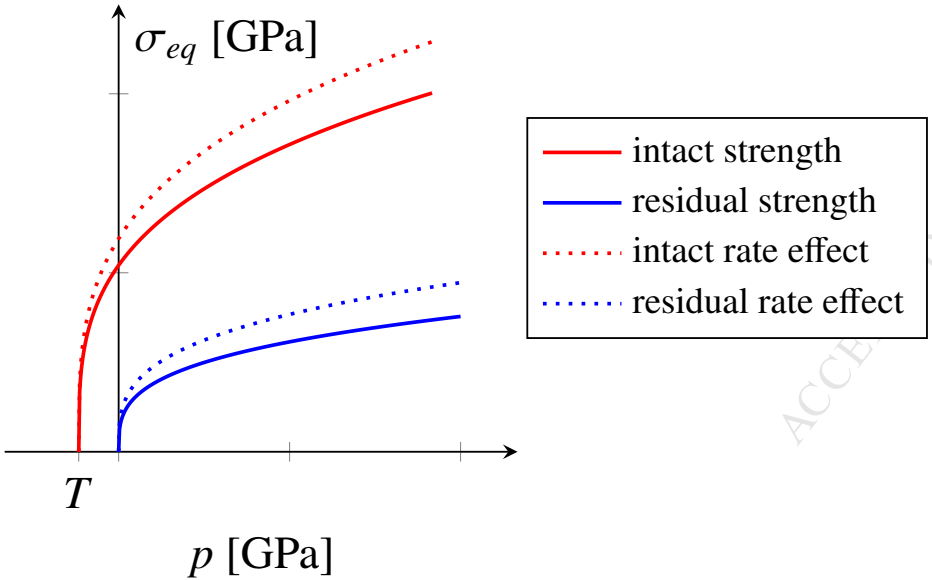

proposed model

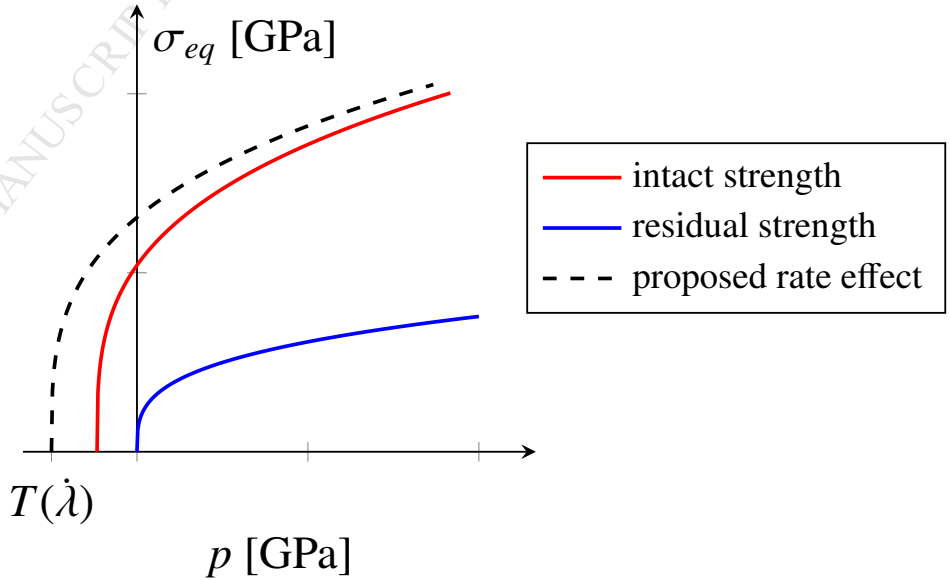

- A modification to the Johnson-Holmquist-2 ceramic material model is proposed
- Viscosity is included on the hydrostatic tensile strength to provide regularization
- The proposed model is shown to regularize under quasi-static and dynamic loading
- A mixed linear/logarithmic viscosity formulation limits the failure zone size